



저작자표시-비영리-변경금지 2.0 대한민국

이용자는 아래의 조건을 따르는 경우에 한하여 자유롭게

- 이 저작물을 복제, 배포, 전송, 전시, 공연 및 방송할 수 있습니다.

다음과 같은 조건을 따라야 합니다:



저작자표시. 귀하는 원저작자를 표시하여야 합니다.



비영리. 귀하는 이 저작물을 영리 목적으로 이용할 수 없습니다.



변경금지. 귀하는 이 저작물을 개작, 변형 또는 가공할 수 없습니다.

- 귀하는, 이 저작물의 재이용이나 배포의 경우, 이 저작물에 적용된 이용허락조건을 명확하게 나타내어야 합니다.
- 저작권자로부터 별도의 허가를 받으면 이러한 조건들은 적용되지 않습니다.

저작권법에 따른 이용자의 권리는 위의 내용에 의하여 영향을 받지 않습니다.

이것은 [이용허락규약\(Legal Code\)](#)을 이해하기 쉽게 요약한 것입니다.

[Disclaimer](#)

**Thesis for the Degree of Master of Engineering**

**One-step synthesis of g-C<sub>3</sub>N<sub>4</sub> nanosheets with  
improved photocatalytic performance for  
organic dye degradation under visible light  
irradiation**

by

**HOANG THI LAN ANH**

**Department of Environmental Engineering**

**The Graduate School**

**Pukyong National University**



**August, 2022**

**One-step synthesis of g-C<sub>3</sub>N<sub>4</sub>  
nanosheets with improved  
photocatalytic performance for organic  
dye degradation under visible light  
irradiation**

**Advisor: Prof. Tae Yoon Lee**

by

**HOANG THI LAN ANH**

**thesis submitted in partial fulfillment of the requirements**

**for the degree of**

**Master of Engineering**

**in Department of Environmental Engineering, The Graduate School,**

**Pukyong National University**

**August 2022**

**One-step synthesis of g-C<sub>3</sub>N<sub>4</sub> nanosheets with improved photocatalytic performance for organic dye degradation under visible light irradiation**

**A dissertation**

**by**

**HOANG THI LAN ANH**

Approved by:



\_\_\_\_\_  
(Chairman) Prof. Il Gyu Kim

\_\_\_\_\_  
(Member) Prof. Joon Yeob Lee

\_\_\_\_\_  
(Member) Prof. Tae Yoon Lee

**August 26th, 2022**

# CONTENTS

ABSTRACT.....	viii
CHAPTER 1: INTRODUCTION .....	1
1.1 Introduction of photocatalyst.....	1
1.2 Introduction of graphitic g-C <sub>3</sub> N <sub>4</sub> .....	5
1.3 Scope of the research .....	9
1.4 Organization of the Thesis .....	9
CHAPTER 2: MATERIALS AND EXPERIMENTS .....	10
2.1 Materials.....	10
2.2 Synthesis of catalysts.....	10
2.2.1 Synthesis of bulk g-C <sub>3</sub> N <sub>4</sub> .....	10
2.2.2 Synthesis of CN-nanosheets using melamine and ammonium chloride..	11
2.2.3 Synthesis of g-C <sub>3</sub> N <sub>4</sub> modified with different ammonium salts.....	12
2.3 Characterization.....	12
2.4 Photocatalytic activity test for rhodamine B .....	13
2.5 Active species trapping experiments.....	13
CHAPTER 3: RESULTS AND DISCUSSION .....	14
3.1 Characterization.....	14
3.1.1 CN-Nanosheets .....	14
3.1.2 g-C <sub>3</sub> N <sub>4</sub> modified using different ammonium salts .....	22
3.2 Photocatalytic activity test .....	29
3.2.1 CN-nanosheets for degradation Rhodamine B under visible light.....	29
3.2.2 g-C <sub>3</sub> N <sub>4</sub> modified using different ammonium salts .....	42
CHAPTER 4: CONCLUSION.....	56
REFERENCES.....	59

## LIST OF FIGURES

Figure 1.1 The basic principle of a photocatalytic reaction. ....	3
Figure 1.2 (A) Triazine and (B) tri-s-triazine (heptazine) structures of g-C <sub>3</sub> N <sub>4</sub> . ....	6
Figure 1.3 Summarize the synthesis process of g-C <sub>3</sub> N <sub>4</sub> by thermal polymerization of different precursors. ....	7
Figure 2.1 Scheme of synthesis bulk g-C <sub>3</sub> N <sub>4</sub> . ....	11
Figure 2.2 Scheme of synthesis g-C <sub>3</sub> N <sub>4</sub> nanosheets. ....	12
Figure 3.1 TEM images of (a) CN-Bulk and (b) CN-nanosheets. ....	14
Figure 3.2 XRD patterns of as-prepared samples. ....	15
Figure 3.3 FTIR spectra of CN-bulk and CN-nanosheets. ....	16
Figure 3.4 UV-vis absorption spectra. ....	18
Figure 3.5 Estimated band gaps of CN-bulk and CN-nanosheets. ....	18
Figure 3.6 Figure 3.6 PL emission spectra under excitation at 360 nm. ....	20
Figure 3.7 Gaussian peak fitting of two samples PL emissions spectrums. ....	21
Figure 3.8 The proposed formation process of g-C <sub>3</sub> N <sub>4</sub> nanosheets. ....	22
Figure 3.9 TEM images of four samples using different ammonium salts. ....	23
Figure 3.10 XRD pattern of four as-prepared samples. ....	24
Figure 3.11 FTIR spectra of four as-prepared samples. ....	25
Figure 3.12 UV-visible absorption spectra. ....	26
Figure 3.13 Estimated band gap of four as-prepared samples. ....	27
Figure 3.14 PL spectra of four as-prepared samples. ....	28
Figure 3.15 Gaussian peak fitting of four samples. ....	29
Figure 3.16 Photodegradation rate of RhB under visible light. Condition experimental: [Catalyst] = 0.5 gL <sup>-1</sup> , [RhB] = 20 mgL <sup>-1</sup> , V= 25 mL, Light wavelength > 400 nm. ....	30
Figure 3.17 The absorption of RhB on the catalyst surface. Condition experimental: [Catalyst] = 0.5 gL <sup>-1</sup> , [RhB] = 20 mgL <sup>-1</sup> , V= 25 mL, Light wavelength > 400 nm. ....	31
Figure 3.18 The UV-vis spectrum of RhB solution at interval time. Condition experimental: [Catalyst] = 0.5 gL <sup>-1</sup> , [RhB] = 20 mgL <sup>-1</sup> , V= 25 mL, Light wavelength > 400 nm. ....	32
Figure 3.19 First-order kinetic for photodegradation of RhB under visible light. Condition experimental: [Catalyst] = 0.5 gL <sup>-1</sup> , [RhB] = 20 mgL <sup>-1</sup> , V= 25 mL, Light wavelength > 400 nm. ....	34
Figure 3.20 Effect of catalyst dosage on photodegradation of Rhodamine B. Condition experimental: [Catalyst] = 0.5 gL <sup>-1</sup> , [RhB] = 20 mgL <sup>-1</sup> , V= 25 mL, Light wavelength > 400 nm. ....	35
Figure 3.21 Effect of initial concentration of RhB on the photodegradation rate. Condition experimental: [Catalyst] = 0.5 gL <sup>-1</sup> , [RhB] = 20 mgL <sup>-1</sup> , V= 25 mL, Light wavelength > 400 nm. ....	36

Figure 3.22 Effect of pH on the photodegradation rate of RhB under visible light. Condition experimental: [Catalyst] = 0.5 gL <sup>-1</sup> , [RhB] = 20 mgL <sup>-1</sup> , V= 25 mL, Light wavelength > 400 nm. ....	37
Figure 3.23 Photodegradation rate of CN-nanosheets over 4 cycles. Condition experimental: [Catalyst] = 0.5 gL <sup>-1</sup> , [RhB] = 20 mgL <sup>-1</sup> , V= 25 mL, Light wavelength > 400 nm. ....	38
Figure 3.24 The XRD pattern of CN-nanosheets before and after over 4 cycles. ....	39
Figure 3.25 Active species trapping experiments of CN-nanosheets in degradation. RhB. Condition experimental: [Catalyst] = 0.5 gL <sup>-1</sup> , [RhB] = 20 mgL <sup>-1</sup> , V= 25 mL, Light wavelength > 400 nm. ....	40
Figure 3.26 The proposed mechanism for photodegradation of RhB using g-C <sub>3</sub> N <sub>4</sub> nanosheets when exposed under visible light exposure. ....	42
Figure 3.27 Photodegradation rate of Rhodamine B using four as-prepared samples under visible light. Condition experimental: [Catalyst] = 0.5 gL <sup>-1</sup> , [RhB] = 20 mgL <sup>-1</sup> , V= 25 mL, Light wavelength > 400 nm. ....	43
Figure 3.28 Absorption of Rhodamine B on the catalyst surface Condition experimental: [Catalyst] = 0.5 gL <sup>-1</sup> , [RhB] = 20 mgL <sup>-1</sup> , V= 25 mL, Light wavelength > 400 nm. ....	44
Figure 3.29 The UV-vis spectrum of Rhodamine B solution at interval time. Condition experimental: [Catalyst] = 0.5 gL <sup>-1</sup> , [RhB] = 20 mgL <sup>-1</sup> , V= 25 mL, Light wavelength > 400 nm. ....	45
Figure 3.30 First-order kinetic curves for photodegradation of Rhodamine B under visible light. Condition experimental: [Catalyst] = 0.5 gL <sup>-1</sup> , [RhB] = 20 mgL <sup>-1</sup> , V= 25 mL, Light wavelength > 400 nm. ....	46
Figure 3.31 Effect of CN-(NH <sub>4</sub> ) <sub>2</sub> SO <sub>4</sub> dosage on the photodegradation rate of RhB. Condition experimental: [Catalyst] = 0.5 gL <sup>-1</sup> , [RhB] = 20 mgL <sup>-1</sup> , V= 25 mL, Light wavelength > 400 nm. ....	48
Figure 3.32 Effect of initial concentration Rhodamine B for photodegradation rate under visible light. Condition experimental: [Catalyst] = 0.5 gL <sup>-1</sup> , [RhB] = 20 mgL <sup>-1</sup> , V= 25 mL, Light wavelength > 400 nm. ....	49
Figure 3.33 Effect of pH on photodegradation of Rhodamine B. Condition experimental: [Catalyst] = 0.5 gL <sup>-1</sup> , [RhB] = 20 mgL <sup>-1</sup> , V= 25 mL, Light wavelength > 400 nm. ....	50
Figure 3.34 Photodegradation rate of Rhodamine B over 4 cycles using CN-(NH <sub>4</sub> ) <sub>2</sub> SO <sub>4</sub> . Condition experimental: [Catalyst] = 0.5 gL <sup>-1</sup> , [RhB] = 20 mgL <sup>-1</sup> , V= 25 mL, Light wavelength > 400 nm. ....	51
Figure 3.35 XRD pattern of CN-(NH <sub>4</sub> ) <sub>2</sub> SO <sub>4</sub> before and after over 4 cycles. ....	52
Figure 3.36 Active species trapping experiments of CN-(NH <sub>4</sub> ) <sub>2</sub> SO <sub>4</sub> in degradation Rhodamine B. Condition experimental: [Catalyst] = 0.5 gL <sup>-1</sup> , [RhB] = 20 mgL <sup>-1</sup> , V= 25 mL, Light wavelength > 400 nm. ....	53

Figure 3.37 The proposed mechanism for photodegradation RhB using CN-  
(NH<sub>4</sub>)<sub>2</sub>SO<sub>4</sub> when exposed under visible light exposure.....55



## LIST OF TABLES

Table 1 List of chemicals.....	10
Table 2: Comparison CN-bulk and CN-nanosheets .....	34
Table 3 Comparison of four as-prepared samples .....	47



# 가시광선 조사에서 유기 염료 분해에 대한 광촉매 성능이 개선된 g-C<sub>3</sub>N<sub>4</sub> 나노시트의 1 단계 합성

호양티란안

환경공학과

대학원

부경대학교

## 요약

흑연질화탄소(g-C<sub>3</sub>N<sub>4</sub>)는 다양한 응용 가능성으로 인해 가시광선 반응 광촉매로 많은 관심을 받고 있습니다. 그러나 광생성 전자-정공 쌍의 빠른 재결합과 낮은 비표면적 때문에 활성이 기대에 미치지 못했다. 이러한 문제를 해결하기 위해 귀금속 도핑, g-C<sub>3</sub>N<sub>4</sub> 기반의 이중 구조를 갖는 나노복합체 구성 및 그 형태 제어와 같은 많은 연구가 개발되었습니다. 이러한 방법에서 형태 제어는 비표면적을 증가시킬 수 있기 때문에 g-C<sub>3</sub>N<sub>4</sub> 광촉매의 효율을 높이는 유용한 접근 방식으로 간주되었습니다. 예를 들어, 연구원들은 g-C<sub>3</sub>N<sub>4</sub> 벌크를 사용하여 경질 또는 연질 템플릿 또는 화학적 에칭을 사용하여 열 에칭 및 초음파 보조와 같은 여러 방법을 사용하여 g-C<sub>3</sub>N<sub>4</sub> 나노시트를 준비했습니다. 벌크 g-C<sub>3</sub>N<sub>4</sub> 에 비해 g-C<sub>3</sub>N<sub>4</sub> 나노시트는 더 놀라운 광촉매 성능을 보입니다. 우리 연구에서 g-C<sub>3</sub>N<sub>4</sub> 나노시트는 NH<sub>4</sub>Cl, (NH<sub>4</sub>)<sub>2</sub>SO<sub>4</sub>, CH<sub>3</sub>COONH<sub>4</sub>와 같은 암모늄염의 존재하에 멜라민의 1 단계 열처리에 의해 합성되었습니다. 모든 g-C<sub>3</sub>N<sub>4</sub>

샘플의 표면 형태 및 광학적 특성은 X 선 회절(XRD), 푸리에 변환 적외선 분광법(FTIR), 투과 전자 현미경(TEM), UV 가시광 확산 반사 분광법으로 특성화되었습니다. 합성된 g-C<sub>3</sub>N<sub>4</sub> 나노시트는 벌크 g-C<sub>3</sub>N<sub>4</sub>와 비교하여 210 분 후 약 98% RhB 제거로 가시광선 조사에서 우수한 광촉매 성능을 나타냈다. 촉매 투여량, pH, RhB 농도가 g-C<sub>3</sub>N<sub>4</sub> 나노시트의 광촉매 활성 효율에 미치는 영향도 조사하였다. 소거 실험에 따르면 h<sup>+</sup> 및 ·O<sub>2</sub><sup>-</sup> 종은 RhB에 대한 중요한 반응성 종으로 간주되었습니다. 따라서 우리의 조사는 환경 오염 제거를 위한 높은 비표면적을 갖는 g-C<sub>3</sub>N<sub>4</sub> 나노시트를 구성하는 쉽고 효율적인 방법을 제공할 수 있습니다.



# One-step synthesis of g-C<sub>3</sub>N<sub>4</sub> nanosheets with improved photocatalytic performance for organic dye degradation under visible light irradiation

Hoang Thi Lan Anh

Department of Environmental Engineering

The Graduate School

Pukyong Nation University

## ABSTRACT

Graphitic carbon nitrides (g-C<sub>3</sub>N<sub>4</sub>) have received much attention as a visible-light respond photocatalyst due to a wide range of possible application. However, its activity could not meet expectations due to the fast of recombination of photogenerated electron-hole pairs and low specific surface area. Many studies have developed to solve these issues, such as doping with a noble metal, constructing nanocomposites with heterostructures based on g-C<sub>3</sub>N<sub>4</sub>, and controlling its morphologies. In these methods, morphology control has been considered a valuable approach for enhancing the efficiency of g-C<sub>3</sub>N<sub>4</sub> photocatalyst because its specific surface area can be increased. For example, researchers used g-C<sub>3</sub>N<sub>4</sub> bulk to prepare g-C<sub>3</sub>N<sub>4</sub> nanosheets using several methods, such as thermal etching and ultrasonic-assisted, using hard or soft templates or chemical etching. Compared to bulk g-C<sub>3</sub>N<sub>4</sub>, g -C<sub>3</sub>N<sub>4</sub> nanosheets have more incredible photocatalytic performance. In our study, g-C<sub>3</sub>N<sub>4</sub> nanosheets were synthesized by a one-step thermal treatment of melamine in the presence of ammonium salts such as NH<sub>4</sub>Cl, (NH<sub>4</sub>)<sub>2</sub>SO<sub>4</sub>, CH<sub>3</sub>COONH<sub>4</sub>. The characterizations about surface morphology and optical properties of all g-C<sub>3</sub>N<sub>4</sub> samples were investigated by X-ray diffraction (XRD), Fourier transform infrared spectroscopy (FTIR), transmission electron microscopy (TEM),

UV-visible diffuse reflectance spectroscopy. The as-synthesized g-C<sub>3</sub>N<sub>4</sub> nanosheets exhibited excellent photocatalytic performance under visible light irradiation with about 98% RhB removal after 210 min compared to bulk g-C<sub>3</sub>N<sub>4</sub>. The effect of catalyst dosage, pH, concentration of RhB on the degradation efficiency using g-C<sub>3</sub>N<sub>4</sub> nanosheets was also investigated. According to the scavenging experiment, h<sup>+</sup> and <sup>•</sup>O<sub>2</sub><sup>-</sup> species were demonstrated as the critical reactive species for the RhB. Therefore, our investigation may provide a facile and efficient way to synthesize the g-C<sub>3</sub>N<sub>4</sub> nanosheets with a high specific surface area for environmental decontamination.



# Acknowledgement

Firstly, I would like to express my deepest gratitude to my advisor, Prof. Tae-Yoon Lee, who awarded me the opportunity to study and research in Development of Photocatalyst Lab, Pukyong National University. I would like to give sincere thanks to him for his enthusiasm, valuable and patient guidance during my master course

Secondly, I would like to thank another member in my laboratory. Dr. Trinh Nguyen Duy, a postdoc in my laboratory for his helpful comments and discussions on this study. He always encouraged me, put forward many useful suggestions. Mr. Nhat Le Duy, a labmate, who learn many things with me and helps each other during the project and spent a perfect unforgettable time together.

Thirdly, I would like to thank to Professor Il Gyu Kim and Professor Joon Yeob Lee, committees of this dissertation, for their helpful suggestions and recommendations as well as their valuable comments.

Fourthly, I would like to thank to the other Professor from Department of Environmental Engineering, Pukyong National University for many valuable lectures. These lectures not only enlarge my knowledge horizon but also motivate me to keep going on the research journey.

Finally, my sincere gratitude goes to my family for always supporting me, to all my friends in PKNU for the great help and unforgettable moments we shared. Without them, my study journey would not have been possible.

**Busan 2022, July**

**Hoang Thi Lan Anh**

# CHAPTER 1: INTRODUCTION

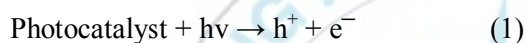
## 1.1 Introduction of photocatalyst

With the rapid growth of urbanization and industrialization, people's demand on resources has increased. This development leads to a slew of energy shortages and environmental issues. Semiconductor photocatalytic technology has received much interest because it can be use solar energy to generate hydrogen and degrade organic pollutants into  $\text{CO}_2$  and  $\text{H}_2\text{O}$  [1]. Since the generation of hydrogen via water splitting using  $\text{TiO}_2$  was applied by the report of Fujishima and Honda in 1972 [2], many works were conducted to use  $\text{TiO}_2$  as a photocatalyst. These efforts extended the application of photocatalyst and drew significant research attention [3]. The direct of research about photocatalyst can be divided into four main directions: photocatalytic hydrogen generation, photocatalytic reduction of  $\text{CO}_2$ , photocatalyst wastewater treatment [4]. Photocatalyst can be used to treat contaminants in both water and air and its properties are stable during the reaction time. Moreover, the photocatalyst can also perform in room temperature and use solar or artificial light.

Nowadays, heterogeneous photocatalysis with semiconductors plays a vital role in facing new global environment and energy-related issues [5]. A photocatalytic reaction of semiconductors is described as a chemical reaction that occurs in the presence of light and a photocatalyst substance [4]. This reaction owned many advantages, such as producing hydrogen, degradation of organic pollutants and no creating secondary pollution. The basic principle of a photocatalytic reaction was shown in [figure 1.1](#)

In photocatalytic reaction, semiconductor materials were irradiation under light. A semiconductor structure consists of a low-energy valence band (VB), a high-energy conduction band (CB), and the band gap which is between a conduction band and valence band. When the energy of incoming light has higher than the energy band gap of semiconductors, the electrons on the valence band are excited and jump to a conductor band and the hole are generated in the valence band [6]. The electrons on

the conduction band will move to the surface of the photocatalyst, after that they take part in a reduction reaction while the hole on the valance band participate in an oxidation reaction. The detailed of photocatalytic mechanism is divided into many stages. Under a certain energy of light, the electrons ( $e^-$ ) are moved to conduction band and the holes ( $h^+$ ) stay in the valance band. The hole ( $h^+$ ) in valance band will react with organic compound and produce  $CO_2$  and  $H_2O$  as end products. Another way, the hole can also participate in oxidation reaction with organic compounds by reacting with water to generate that hydroxyl radical ( $\cdot OH$ ). After,  $\cdot OH$  can convert organic compound to  $CO_2$  and water. The electrons ( $e^-$ ) in the conduction band can react with oxygen and form a radical superoxide ( $O_2^{\cdot -}$ ). The mechanism of semiconductor photocatalyst can be summarized by the following equations:



A critical key to improving photocatalytic activity is the reduce of the rate recombination of electron and hole. In other words, it is critical for successful photocatalytic degradation organic compound that the reduction reaction and oxidation reduction must be occurred simultaneously and the rate of recombination of election-hole pair is limited.

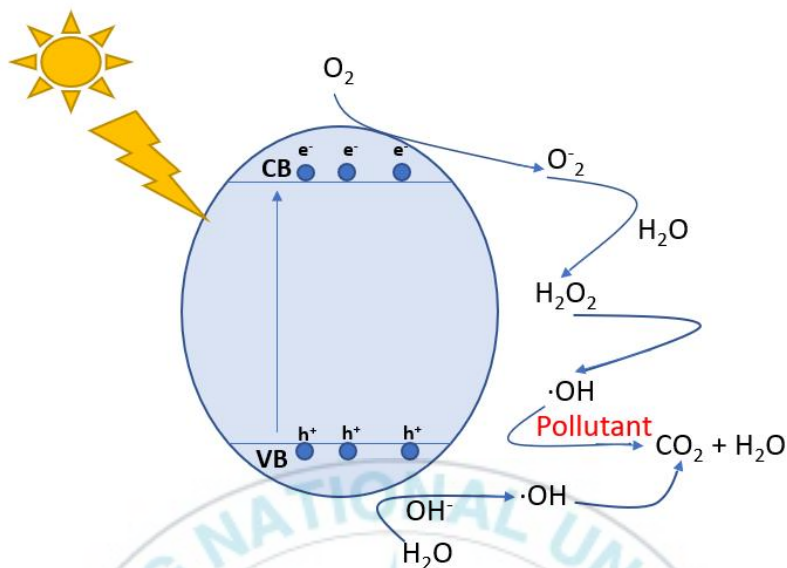


Figure 1.1 The basic principle of a photocatalytic reaction.

The photocatalytic process is extremely complicated and consists of many stages so there are many factors can affect this reaction. The key factors that influence the photocatalytic process are the catalyst dosage, medium condition (pH), the type and concentration of target pollutants, light source, and temperature [7]. Normally, the photocatalytic activity increase with higher catalyst dosage. This can be observed that increasing the amount of catalyst provides a greater number of active sites on the catalyst's surface, resulting in a higher number of  $\text{OH}^\bullet$  radicals participating in organic molecule degradation. However, once the catalyst concentration reaches a particular level, the reaction rate slows down as the catalyst concentration rises [8]. The photocatalytic degradation rate also depends on target pollutants concentration. When the concentration of pollutants changes, the results of degradation rate are different [9]. These findings could be explained by a lack of catalyst surface for the generation of hydroxyl radicals. The high concentration of pollutants caused the decrease in the light penetration [10]. Thus, the time for degradation of pollutant would be longer compared to lower concentration of pollutants. Many researchers also studied about

the influence of pH on the photocatalytic reaction. pH is one of the most important parameters influencing photocatalytic water systems since it defines organic compound chemistry such as charge, acidity-pKa, and partitioning coefficient and influences the charge on the catalyst. The point of zero charge (PZC) was used in some reports to investigate the impact of pH on the photocatalytic oxidation performance [11]. The PZC is the pH of a suspension when the net charge on the surface of an insoluble oxide or hydroxide is zero [12]. Each light sources provide different of light wavelength and light intensity. Light is also a crucial factor in the photocatalytic reaction. When the light intensity increased, the degradation rate of pollutant will be greater. However, increasing the light intensity leads in a significant increase in cost, therefore its practical application may be limited. In some cases, the high light intensity led to waste of energy rather than more degradation of pollutant, so the suitable light intensity is a critical point to save energy and ensure comparable results in all measurements [13]. Much research was studied about the effect of temperature on photocatalytic process. Gaya et al found that the photocatalytic reaction temperature can change the recombination of electron hole charges [14]. Herrmann et al. showed that pollutants can be efficiently adsorbed on the TiO<sub>2</sub> surface at temperatures below 80°C [15].

Among semiconductor materials, titanium dioxide (TiO<sub>2</sub>) is the most extensively used photocatalyst material because of its semiconductor properties, which make it an excellent choice for photocatalysis applications utilizing solar or other sources of irradiation. [16]. TiO<sub>2</sub> has several advantages such as nontoxic, water insolubility, hydrophilic, cheap, and stable. Moreover, it can also be sustained on a variety of substrates, including: fibers, stainless steel, glass, and inorganic materials [17]. This property can allow it to be reuse and apply in practical. In nature, TiO<sub>2</sub> consists of three phases such as rutile, anatase and brookite [18]. In these phases, anatase phase have gotten much interest because of its properties such as high photoactivity, low-cost, stability, and negative conduction band potential [19]. Although, TiO<sub>2</sub> has many advantages compared to other semiconductor photocatalysts, it has a high energy band gap (anatase phase and brookite phase: 3.2 eV and rutile phase: 3.0 eV) which

can only absorb light in the UV region. In general, solar light consists of 5% ultraviolet (UV), 43% visible light and 52% harvesting infrared so TiO<sub>2</sub>, which restricts TiO<sub>2</sub> actual environmental application under visible or solar light irradiation [20]. Further, the fast recombination of electron-hole pairs and the phase transform from anatase phase to rutile phase in high temperature can reduce the photocatalytic activity [21]. To solve these problems, researcher have developed several methods to modify TiO<sub>2</sub> for enhancing its activity under visible light irradiation such as doping metal and nonmetal ion [22], coupling with other semiconductor materials [23] and surface modification with inorganic substances [24]. By substituting oxygen atoms from TiO<sub>2</sub>'s lattice and decreasing its band gap, doping metal/nonmetal ions could increase the absorption light range of TiO<sub>2</sub> from UV to visible [25]. This change results in the enhanced photocatalytic activity of TiO<sub>2</sub>. Similarly, coupling with other semiconductor and modifications surface of TiO<sub>2</sub> also play a critical role to improve the activity of TiO<sub>2</sub>. These different methods have also gotten promising results, however, the development of an alternative photocatalyst which can respond in visible light region are the trend for today' photocatalysts field. Graphitic carbon nitride (g-C<sub>3</sub>N<sub>4</sub>), a suitable alternative, has emerged as the next generation photocatalyst in the field of energy conversion and global pollution. The details of g-C<sub>3</sub>N<sub>4</sub> were discussed in section 1.2

## **1.2 Introduction of graphitic g-C<sub>3</sub>N<sub>4</sub>**

An effective photocatalysts should have an appropriate energy band structure to enable to absorb light and efficient charge transfer. In comparison with others photocatalysts, g-C<sub>3</sub>N<sub>4</sub> have received much attention as a non-metal semiconductor due to its properties such as suitable band gap energy, facile synthesis, and high stability [26]. g-C<sub>3</sub>N<sub>4</sub> is not a new photocatalyst material, in fact, it was first used for H<sub>2</sub> evolution by Wang et al [27]. The C<sub>3</sub>N<sub>4</sub> have seven different phases:  $\alpha$ -C<sub>3</sub>N<sub>4</sub>,  $\beta$ -C<sub>3</sub>N<sub>4</sub>, cubic C<sub>3</sub>N<sub>4</sub>, pseudo cubic C<sub>3</sub>N<sub>4</sub>, g-h-triazine, g-o- triazine and g-h-heptazine with different band gap energy: 5.49, 4.85, 4.30, 4.13, 2.97, and 2.88 eV, respectively [28]. Triazine (C<sub>3</sub>N<sub>3</sub>) and tri-s-triazine/heptazine (C<sub>6</sub>N<sub>7</sub>) rings were discovered to be

the fundamental tectonic units for constructing allotropes of  $g\text{-C}_3\text{N}_4$ . (Figure 1.2). When comparing with  $\text{TiO}_2$ ,  $g\text{-C}_3\text{N}_4$  have a suitable band gap energy 2.7-2.8 eV which make it have visible-light absorption ability. Moreover, the  $g\text{-C}_3\text{N}_4$  also have a stable chemical structure and is not dissolved by acid, alkaline, or organic solvents under ambient conditions.  $g\text{-C}_3\text{N}_4$  is thermally stable up to  $600^\circ\text{C}$  in air and decomposed to C and N upon heating above 600 to  $900^\circ\text{C}$  [29]. With all its properties,  $g\text{-C}_3\text{N}_4$  become a promising photocatalyst which can use for water splitting and decomposition pollutants under visible light irradiation.

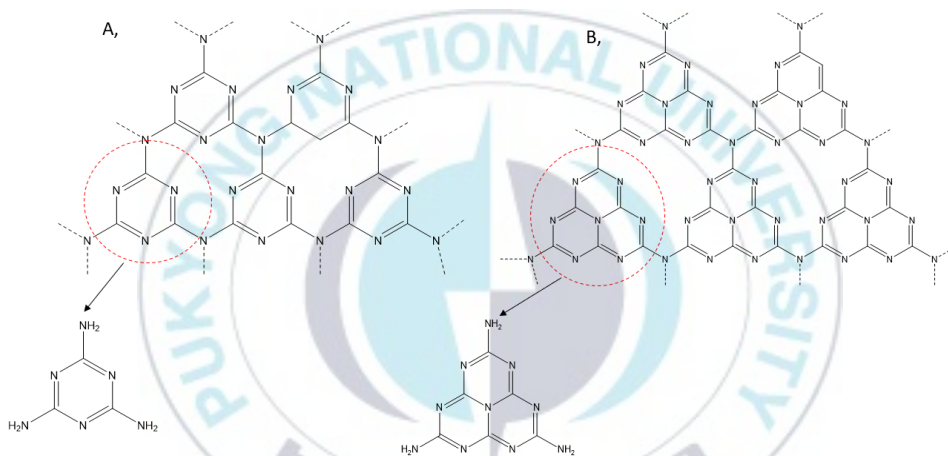
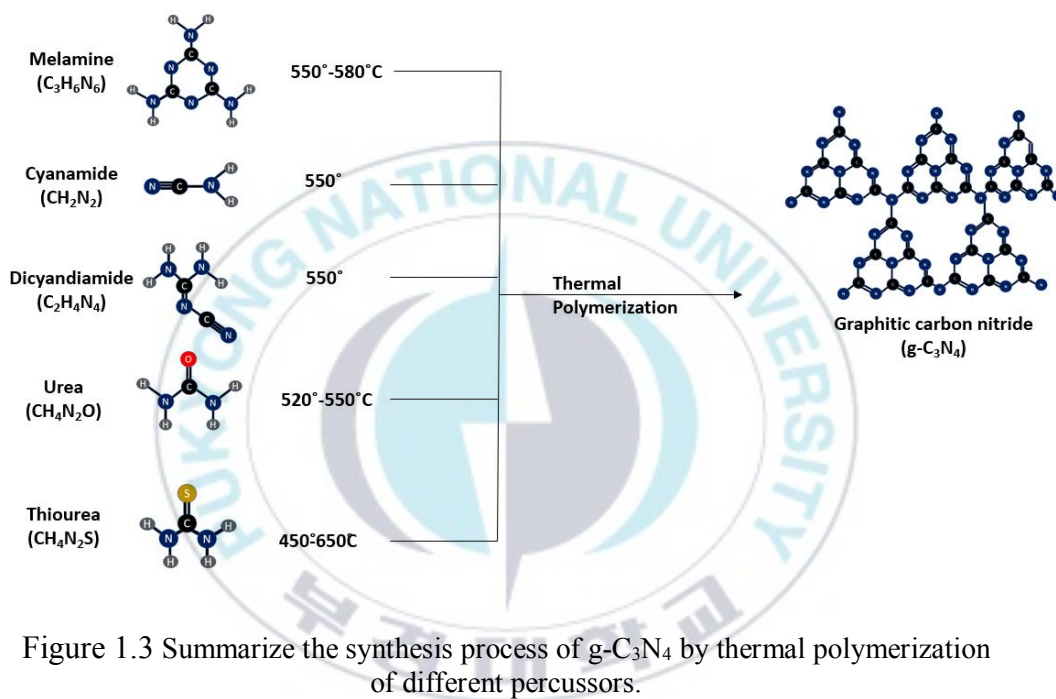


Figure 1.2 (A) Triazine and (B) tri-s-triazine (heptazine) structures of  $g\text{-C}_3\text{N}_4$ .

Because  $g\text{-C}_3\text{N}_4$  was demonstrated as a promising photocatalyst, many efforts were carried out to synthesis  $g\text{-C}_3\text{N}_4$ . In general,  $g\text{-C}_3\text{N}_4$  was often synthesized using nitrogen-rich precursors such as melamine [30], urea [31], thiourea [32], cyanamide [33], and dicyandiamide [34] (Figure 1.3). The  $g\text{-C}_3\text{N}_4$  obtained from different precursors show contradictory photocatalytic performance and the correlation between morphology, surface area, and photoelectrochemical characteristics of  $g\text{-C}_3\text{N}_4$  is frequently incomplete. However, the obtained  $g\text{-C}_3\text{N}_4$  is the bulk materials with several drawbacks such as small surface area, high electron and hole pairs

recombination rate, and low electrical conductivity. To overcome these drawbacks, several strategies have been used to enhance the photocatalytic efficiency of  $g\text{-C}_3\text{N}_4$  such as doping noble metal [35], metal [36], nonmetals [37] or coupling with other semiconductors [38], and controlling morphologies. Among them, controlling the morphology of  $g\text{-C}_3\text{N}_4$  photocatalysts is a potential method since it can expand the material's specific surface area [39].



From previous reports, bulk  $g\text{-C}_3\text{N}_4$  has poor photocatalytic efficiency because of its small surface area and fast electron and hole pairs recombination rate.  $g\text{-C}_3\text{N}_4$  nanosheets obtained from delamination of layered compounds have becoming widely attractive. In  $g\text{-C}_3\text{N}_4$  photocatalysts, nano structural engineering was widely used to adjust the morphology, porosity, structure, surface area, and size of photocatalyst. [40]. Much research about  $g\text{-C}_3\text{N}_4$  nanosheets were carried out to find out an effective synthesis method. Exfoliation technology was developed as a popular method. Zhang et al successful synthesized  $g\text{-C}_3\text{N}_4$  nanosheets from  $g\text{-C}_3\text{N}_4$  bulk by water exfoliation

[41]. Lin et al produced g-C<sub>3</sub>N<sub>4</sub> nanosheets by mixed solvent exfoliation and ultrasonic dispersion for 10 hours [42]. Moreover, the g-C<sub>3</sub>N<sub>4</sub> nanosheets could be prepared by thermal exfoliation method from g-C<sub>3</sub>N<sub>4</sub> bulk. Dong et al prepared CN-nanosheets by directly thermal exfoliation of urea [43]. Niu et al applied thermal oxidation etching of bulk g-C<sub>3</sub>N<sub>4</sub> in air to generate g-C<sub>3</sub>N<sub>4</sub> nanosheet [44]. In general, synthesis of g-C<sub>3</sub>N<sub>4</sub> nanosheets consisted of two steps. Firstly, g-C<sub>3</sub>N<sub>4</sub> bulk would be synthesized from nitrogen-rich precursors. After that, liquid exfoliating, ultrasonic dispersion, or thermal exfoliation in a certain environment, are used to make ultrathin nanosheets.

Many researchers have been focusing on developing a one pot synthesis technique that uses a self-supporting or additive environment as a bubble template to reduce the number of experimental steps and enable large-scale manufacture of g-C<sub>3</sub>N<sub>4</sub> nanosheets. Dong et al prepared g-C<sub>3</sub>N<sub>4</sub> nanosheets by directly thermal treatment of urea through prolonging retention time [45]. Urea is a low-cost and active precursor for synthesis g-C<sub>3</sub>N<sub>4</sub> nanosheets, but this approach has the drawback of a poor yield, which would prevent its application in large scale. For example, Liu et al. were carried out the simple thermal treatment method of urea to synthesis g-C<sub>3</sub>N<sub>4</sub>, but the yield of this experiment was only 4% [46]. Zhang et al synthesized porous g-C<sub>3</sub>N<sub>4</sub> by thermal treatment of dicyandiamide precursor using urea as bubble template [47]. Some research used melamine as precursor, but the yield was not mentioned. Using sublimed sulfur as a soft-template agent, He et al created porous g-C<sub>3</sub>N<sub>4</sub> by heating condensation of melamine [48]. Sun et al synthesized mesoporous g-C<sub>3</sub>N<sub>4</sub> nanosheets from carbonated beverage-reformed commercial melamine [49].

Although, numerous efforts have been employed to produce g-C<sub>3</sub>N<sub>4</sub> nanosheets, almost of the current methods are often low-yield and time-consuming. A new alternative way to obtain g-C<sub>3</sub>N<sub>4</sub> nanosheet with high yield and high photocatalytic efficiency is still very much necessary. In this study, we developed a simple one step method for synthesis g-C<sub>3</sub>N<sub>4</sub> which achieve of high quality and high activity. The raw material used in our study were melamine and different ammonium salts. In

polymerization of melamine at high temperature, ammonium salts released chemical gases which blew polymers into numerous large bubbles and obtained g-C<sub>3</sub>N<sub>4</sub> nanosheets. This method brings several advantages such as economic, scalable production and high activity. The obtained g-C<sub>3</sub>N<sub>4</sub> nanosheets enhanced specific surface area and achieve improved electron transport ability and its characteristics will be investigated in detailed.

### **1.3 Scope of the research**

This objective of this study is to find out a one-step method of synthesis g-C<sub>3</sub>N<sub>4</sub> through thermal polycondensation of melamine with high-yield and high photocatalytic activity. To achieve this objective, the following approaches had been carried out:

- (1) Synthesis g-C<sub>3</sub>N<sub>4</sub> nanosheets by using melamine and ammonium chloride through one-pot synthesis with increased photocatalytic efficiency under visible light.
- (2) Using different ammonium salts in synthesis process of g-C<sub>3</sub>N<sub>4</sub> to study the effect of different ammonium salts to this process.
- (3) Investigating the photocatalytic efficiency of the as-synthesized catalysts through the photodegradation of rhodamine B under visible light.

### **1.4 Organization of the Thesis**

This thesis is divided into four chapters. Chapter 1 is a brief introduction as presented above. In chapter 2, the materials and method for synthesis of catalyst is described. Chapter 3 presents the results of photocatalytic activity test and characterization of as-prepared samples. Chapter 4 summarizes the key findings of this research.

## CHAPTER 2: MATERIALS AND EXPERIMENTS

### 2.1 Materials

The chemicals which were used in this study included in following table:

Table 1 List of chemicals

No	Name of chemical	Chemical formula	Purity	Company
1	Melamine	$C_3H_6N_6$	99.5%	Junsei
2	Ammonium chloride	$NH_4Cl$	99.5%	Junsei
3	Ammonium sulfate	$(NH_4)_2SO_4$	99%	Kanto
4	Ammonium acetate	$CH_3COONH_4$	97%	Junsei
5	Rhodamine B	$C_{28}H_{31}ClN_2O_3$	95%	Sigma-Aldrich
6	Triethanolamine	$C_6H_{15}NO_3$	98%	Sigma-Aldrich
7	p-Benzoquinone	$C_6H_4O_2$	98%	Sigma-Aldrich
8	Isopropyl alcohol	$(CH_3)_2CHOH$	99.5%	Samchun
9	Ethanol	$C_2H_5OH$	99.9%	Duksan
10	Distilled water	$H_2O$		

### 2.2 Synthesis of catalysts

#### 2.2.1 Synthesis of bulk g- $C_3N_4$

Bulk g- $C_3N_4$  powder was produced like a previous study with minor modifications [50]. In detailed, the bulk g- $C_3N_4$  was synthesized following the typical procedure: melamine was placed in a semi-closed alumina crucible with a lid and heated to 550°C with heating rate 10°C min<sup>-1</sup> for 3 h. After cooling to room temperature, the

obtained product was thoroughly washed several time with distilled water and dried at 80°C for 12 h. This obtained sample was donated by CN-bulk.



Figure 2.1 Scheme of synthesis CN-bulk

### 2.2.2 Synthesis of CN-nanosheets using melamine and ammonium chloride

The g-C<sub>3</sub>N<sub>4</sub> nanosheets was synthesized following same condition of the bulk by using melamine and ammonia chloride. Firstly, equal amounts of melamine and ammonium chloride were mixed in an agate mortar. The key to success for this method is fully mixed. Next, the mixture was placed into a crucible with a lid and calcined in a furnace at 550°C for 3 h with a heating rate of 10°C min<sup>-1</sup>. After cooling the obtain product to room temperature, it was crushed into powder. Lastly, the powder was washed many times using distilled water and dried by vacuum drier at 80°C for 12 h. The g-C<sub>3</sub>N<sub>4</sub> nanosheets was donated by CN-nanosheets.

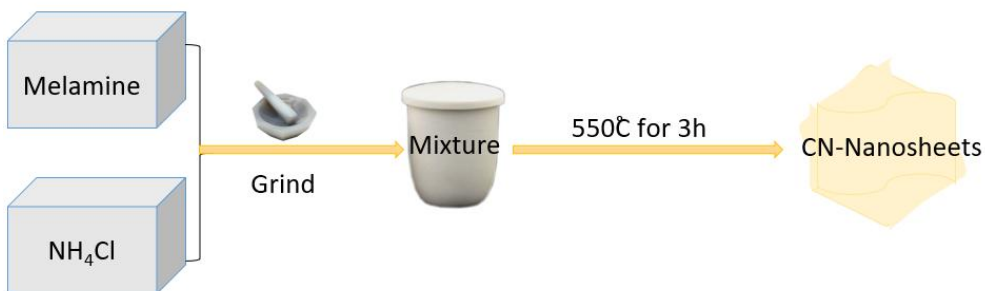


Figure 2.2 Scheme of synthesis CN- nanosheets.

### 2.2. 3 Synthesis of g-C<sub>3</sub>N<sub>4</sub> modified with different ammonium salts.

The g-C<sub>3</sub>N<sub>4</sub> modified with different ammonium salts were carried out under the same condition with CN-nanosheets from melamine and ammonium chloride by using ammonium sulfate and ammonium acetate substitute ammonium chloride. The obtained products from ammonium sulfate and ammonium acetate were donated as CN-(NH<sub>4</sub>)<sub>2</sub>SO<sub>4</sub> and CN-CH<sub>3</sub>COONH<sub>4</sub>, respectively.

### 2.3 Characterization

The crystalline structure of the obtained g-C<sub>3</sub>N<sub>4</sub> samples were analyzed using X-ray diffractometer (XRD) (Rigaku (Ultima IV)). The morphology was measured by a transmission electron microscope (TEM, JEOL(JEM-F200)). Fourier transform infrared spectroscopy (Bruker (CARY 600)) was used for investigating the chemical bonding status. UV-visible spectrometer (JASCO (V-670)) were used to measure ultraviolet-visible (UV-vis) absorption spectra of the sample. Photoluminescence spectra (PL) were measured using a fluorescence spectrometer (Horiba (Fluorolog-QM)).

## 2.4 Photocatalytic activity test for rhodamine B

To investigate photocatalytic efficiency of all the samples, the photocatalytic decomposition of rhodamine B (RhB, 20 mg L<sup>-1</sup>) under visible light were measured using a 300W Xe-arc lamp and 400 nm UV cut-off filter. Before the light was turned on, 12.5 mg catalyst was dispersed with 25 ml RhB solution (20 mg L<sup>-1</sup>) and magnetic stirred. During photocatalytic process, 1ml of solution was taken at time interval of (0, 15, 30, 60, 90, 150 and 210) min. The suspension was filtered using 0.22 mm PTPE filter to eliminate solid particles. The decrease in the concentration of RhB solution at time t is measured using UV-vis spectrophotometer at maximum wavelength 554 nm. The efficiency (H) of organic dye was calculated by the following equation:

$$H(\%) = \left(1 - \frac{C_t}{C_0}\right) \times 100 \quad (6)$$

where, C<sub>0</sub> is the initial concentration of RhB, and C<sub>t</sub> is the concentration of RhB at time t (min).

## 2.5 Active species trapping experiments

The degradation of Rhodamine B is caused by active species generated during the photocatalytic process, such as h<sup>+</sup>, O<sub>2</sub><sup>•-</sup>, and OH<sup>•</sup>, which can be detected using an indirect chemical probe method. Isopropyl alcohol (IPA), triethanolamine (TEA) and benzoquinone (BQ) were used as OH<sup>•</sup>, h<sup>+</sup>, and O<sub>2</sub><sup>•-</sup> scavenger [51]. The experiment was carried out with the same procedure to the above photocatalytic experiments in the presence of chemical agents. The chemical agents were added before the beginning of the photocatalytic experiment. The concentration of IPA and TEA were 0.1 M while the concentration of BQ was 10<sup>-3</sup> M because the concentration of RhB maybe difficult to determine by UV-vis spectra with higher concentration of BQ [52].

## CHAPTER 3: RESULTS AND DICUSSION

### 3.1 Characterization

#### 3.1.1 CN-Nanosheets

The morphology of CN-bulk and CN-nanosheets samples were studied by TEM and shown in [figure 3.1](#). The CN-nanosheets are transparent to electron beams due to their thinner layer than CN-bulk [53]. Furthermore, the basic sheet edges roll up to minimize the surface-energy of the sheet which trends similarly to previous study of Niu et al [54].

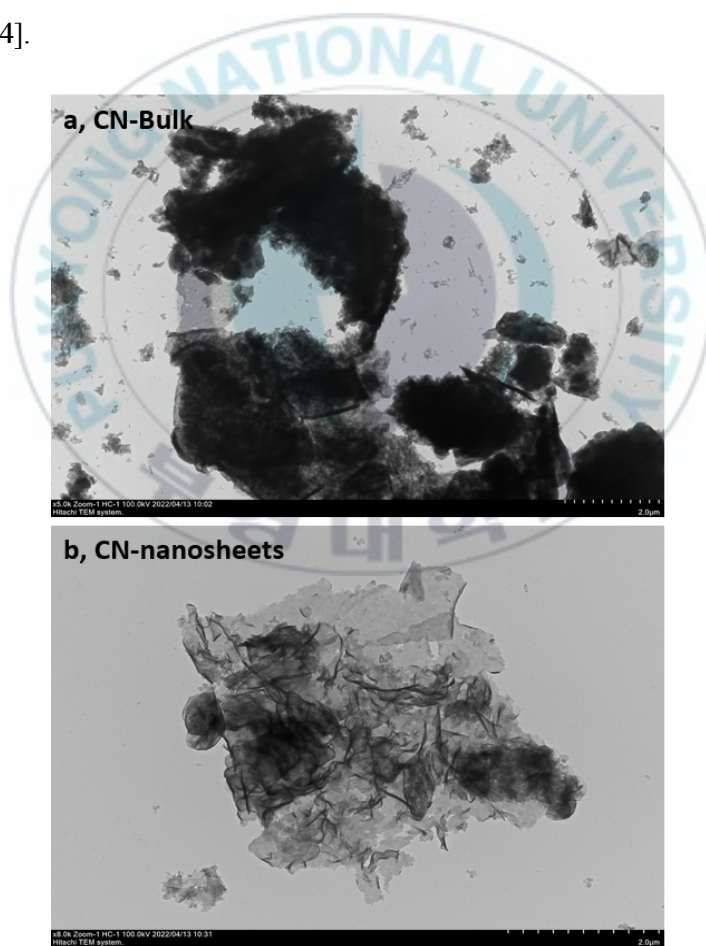


Figure 3.1 TEM images of (a) CN-Bulk and (b) CN-nanosheets

The XRD patterns are shown in the [figure 3.2](#). The XRD pattern of CN-nanosheets revealed two distinct diffraction peaks which are at around  $13^\circ$  and  $27.4^\circ$ . These two peaks are compatible with the graphite-like hexagonal phase of  $g\text{-C}_3\text{N}_4$  previously study. [55]. These peaks indicated the as-prepared samples have the same crystal structure of  $g\text{-C}_3\text{N}_4$ . The low peak corresponds the (100) plane at about  $13.0^\circ$  corresponds to the structural stacking of tri-s-triazine units in the plane [56]. The inter-layer stacking of conjugated aromatic systems is responsible for the typically dominant peak approximately  $27.4^\circ$  ascribed to the (002) plane [57]. The (002) crystal plane corresponds to a sharp diffraction peak in the CN-bulk at  $27.45^\circ$  while for CN-nanosheets, the peak moved to  $27.49^\circ$ . That means that a shortened gallery distance between the basic layer unit and could demonstrate that CN-nanosheets were formed during the heat treatment of melamine and  $\text{NH}_4\text{Cl}$  [58]. The peak's intensity rapidly decreases, indicating that the crystallinity of CN-nanosheets is lower than that of CN-bulk [59]. Besides that, the peak (100) down-shifts from  $12.9^\circ$  to  $12.7^\circ$ , corresponding to an increase of the in-planar hole to hole distance, which ascribed to the promoted planarization of  $g\text{-C}_3\text{N}_4$  layers [33].

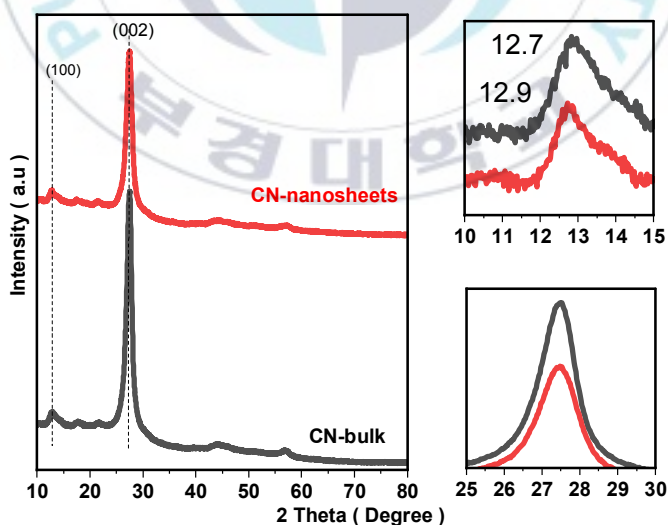


Figure 3.2 XRD patterns of as-prepared samples.

To investigate the surface functional group of the as-prepared CN-bulk and CN-nanosheets, FT-IR spectroscopy were studied in the range 700–4000  $\text{cm}^{-1}$  (Figure 3.3). In general, there is no great difference between CN-bulk and CN-nanosheets in the characteristic FT-IR spectra. These spectra confirmed that the CN-nanosheets still maintained the same chemical structure as the bulk  $\text{g-C}_3\text{N}_4$  [60]. In detail, the broad peaks between 3000  $\text{cm}^{-1}$  and 3500  $\text{cm}^{-1}$  represents N–H stretching[61]. The set of peaks between 1200  $\text{cm}^{-1}$  and 1600  $\text{cm}^{-1}$  are the vibrational absorption of aromatic C–N heterocyclic units [62]. The sharp peak at round 800  $\text{cm}^{-1}$  is the characteristic peak of the tri-s-triazine units which also confirmed in XRD spectrum [63]. According to the above observations, the crystal structure and chemical composition of the CN-nanosheets as synthesized are largely like those of bulk  $\text{g-C}_3\text{N}_4$ .

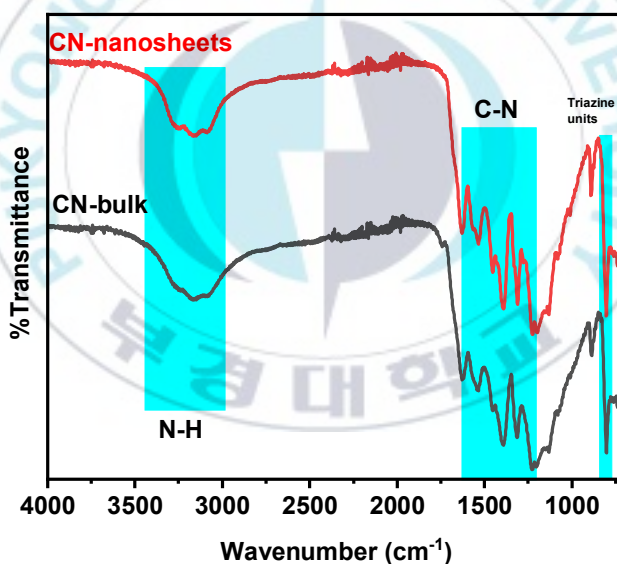


Figure 3.3 FTIR spectra of CN-bulk and CN-nanosheets.

To study the optical performance of CN-bulk and CN-nanosheets, UV-vis DRS was used. The UV-Vis DRS spectrum of the as-prepared was shown in figure 3.4. The absorption thresholds of the as-prepared samples (CN-bulk and CN-nanosheets)

occurs at 471 and 462 nm. This suggests that both CN-bulk and CN-nanosheets have ability to efficiently utilize under visible light [64]. The optical absorption performance of the as synthesized photocatalyst can be evaluated using the band gap energy ( $E_g$ ). The Tauc equation can be used to compute  $E_g$  of photocatalysts based on their absorption spectra.[65].

$$\alpha h\nu = A (h\nu - E_g)^{n/2} \quad (7)$$

where  $A$ ,  $\alpha$ ,  $h\nu$  and  $E_g$  are a proportionality constant, the optical absorption coefficient, a photo energy, and the band gap energy, respectively. The value of  $n$  is determined by the type of optical transition that occurs in semiconductors: for direct transitions, the number is 1, whereas for indirect transitions, the value is 4.[66]. Because  $g\text{-C}_3\text{N}_4$  is indirect semiconductor, the value of  $n$  is 4 and the derived bandgaps from the  $(A h\nu)^2$  versus photon-energy plots, as shown in the figure (Figure 3.5) [67]. The band gap energy of CN-bulk and CN-nanosheets were estimated as 2.68 eV and 2.78 eV, respectively. Different band gaps can lead to different band gap levels, which can have a significant impact on the photooxidation and reduction capabilities of  $g\text{-C}_3\text{N}_4$ . Although the CN-nanosheets have larger band gap than CN-bulk, it means that CN-nanosheets has the stronger redox capability than CN-bulk [39].

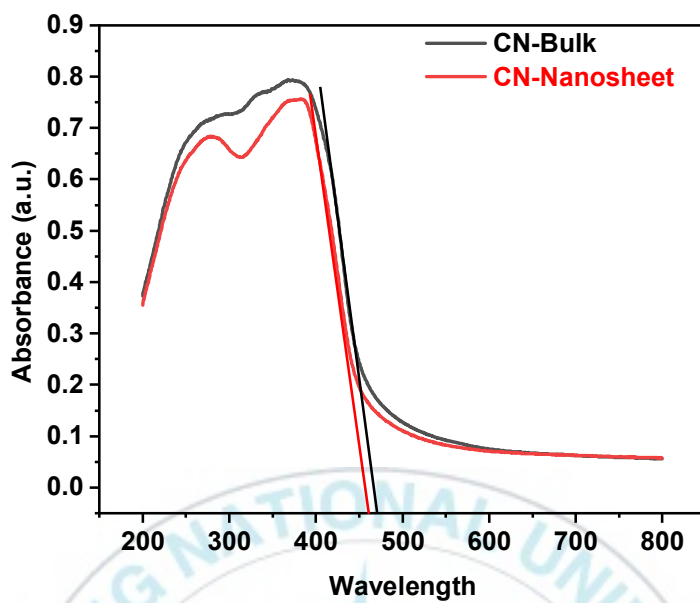


Figure 3.4 UV-vis absorption spectra

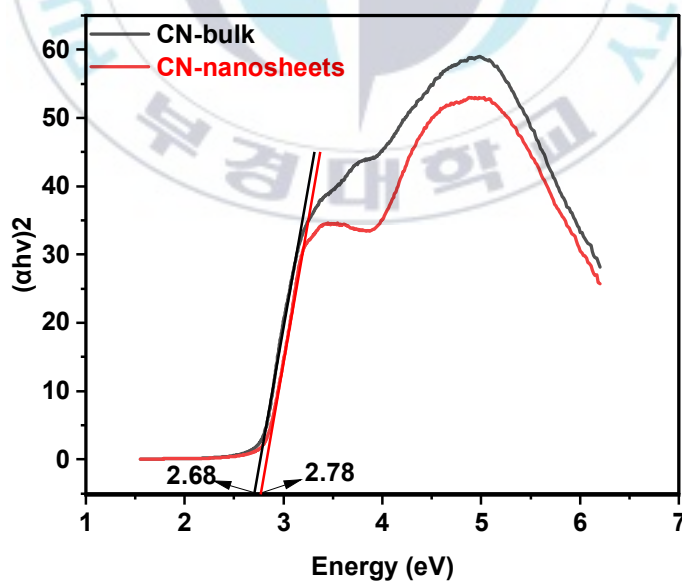


Figure 3.5 Estimated band gaps of CN-bulk and CN-nanosheets.

The rate of photogenerated electrons and holes recombination in as-prepared materials was investigated using PL analysis [68]. The recombination of electron hole pairs can be radiative or non-radiative, and these processes can take diverse paths with or without photon emissions [67]. Charge trapping at defect states within the bandgap is common in nonradiative decays, whereas electron hole recombination only contributes to PL band edge emission when photons are produced with energy near the semiconductor bandgap [68]. The intensity of released photons is determined by the type/structure of the materials and the rate of  $e/h^+$  recombination, with a lower PL emission intensity (at a fixed wavelength near the absorption wavelength) indicating a lesser rate of  $e/h^+$  recombination [69]. The PL spectra of the CN-bulk and CN-nanosheets were excited at 360 nm and presented in the [Figure 3.6](#). The emission peaks of CN-bulk and CN-nanosheets located at around 455 nm and 460 nm which are suitable with the results of DRS measurement. As shown in the figure, the PL emission of CN-bulk is strong in the 450–460 nm region, whereas the emission intensity of CN-nanosheets is much lower than CN-bulk. This change demonstrated that the presence of  $NH_4Cl$  has reduced the electron-hole pair's recombination in the sample.

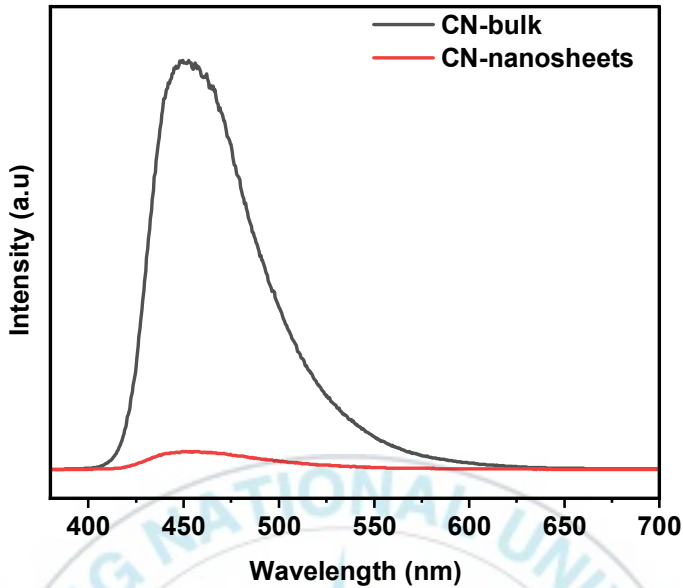


Figure 3.6 Figure 3.6 PL emission spectra under excitation at 360 nm.

All the samples have a broad PL emission that can be divided into three primary Gaussian peaks (Figure 3.7). Three emission peaks at  $P_1$  440 nm,  $P_2$  461 nm, and  $P_3$  499 nm for CN-nanosheets and at  $P_1$  440 nm,  $P_2$  464 nm, and  $P_3$  494 nm for CN-bulk which comes from the recombination of  $e^-/h^+$  from distinct pathways in  $g\text{-C}_3\text{N}_4$ . These recombination paths come from the  $sp^2$  C-N  $\pi$  band,  $sp^3$  C-N  $\sigma$  band, and the lone pair state of the bridge N atom transitions [70]. The  $P_3$  peak position remains approximately 467 nm, owing to the presence of  $\text{NH}_2$  on the edge and a defect of  $\text{C}\equiv\text{N}$  [71]. It was demonstrated further in the above FTIR spectroscopy.

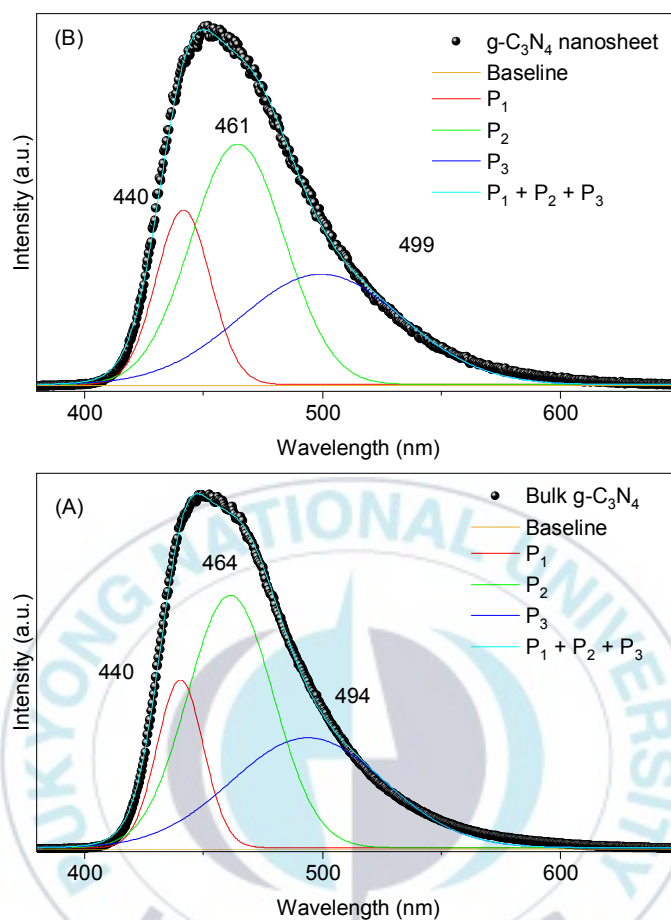


Figure 3.7 Gaussian peak fitting of two samples PL emissions spectra.

The proposed formation process of  $g\text{-C}_3\text{N}_4$  nanosheets is shown in [Figure 3.8](#). In the polymerization of melamine with the increase of temperature,  $\text{NH}_4\text{Cl}$  can be released into the gases  $\text{NH}_3$  and  $\text{HCl}$ . These gases can blow melamine polymers into many large bubbles and result in crinkly  $g\text{-C}_3\text{N}_4$  nanosheets

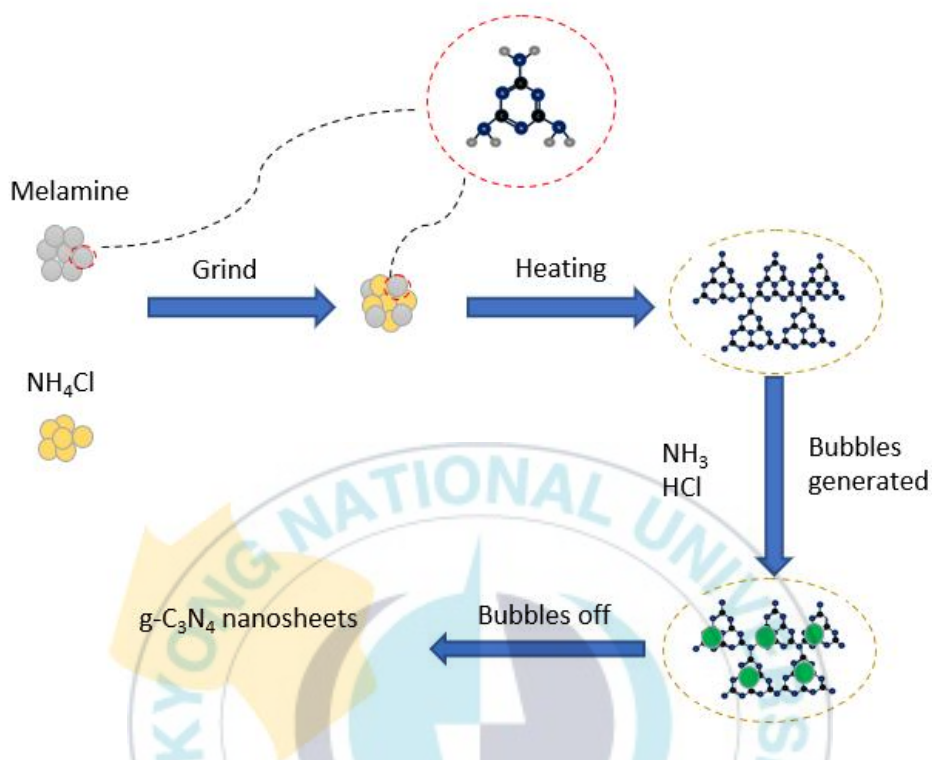


Figure 3.8 The proposed formation process of g-C<sub>3</sub>N<sub>4</sub> nanosheets.

### 3.1.2 g-C<sub>3</sub>N<sub>4</sub> modified using different ammonium salts

To investigate effect of ammonium salts on synthesis process of the as-prepared samples, they are characterized by TEM and shown in figure 3.9. In compared to CN-bulk, all three samples g-C<sub>3</sub>N<sub>4</sub> synthesized in the presence of ammonium salts have a significantly thinner structure, as can be observed in TEM images. When the composite precursors of melamine and ammonium salts were put to the furnace under high temperature, ammonium salts start to decompose and generate gas bubbles such as NH<sub>3</sub>, SO<sub>2</sub>, SO<sub>3</sub>, H<sub>2</sub>O, and HCl, which can be role as dynamic gas template [72]. The nanosheet structure would be formed through the diffusion and explosion of gas bubbles. This structure is expected to provide more active sites, which benefits photocatalytic efficiency [73].

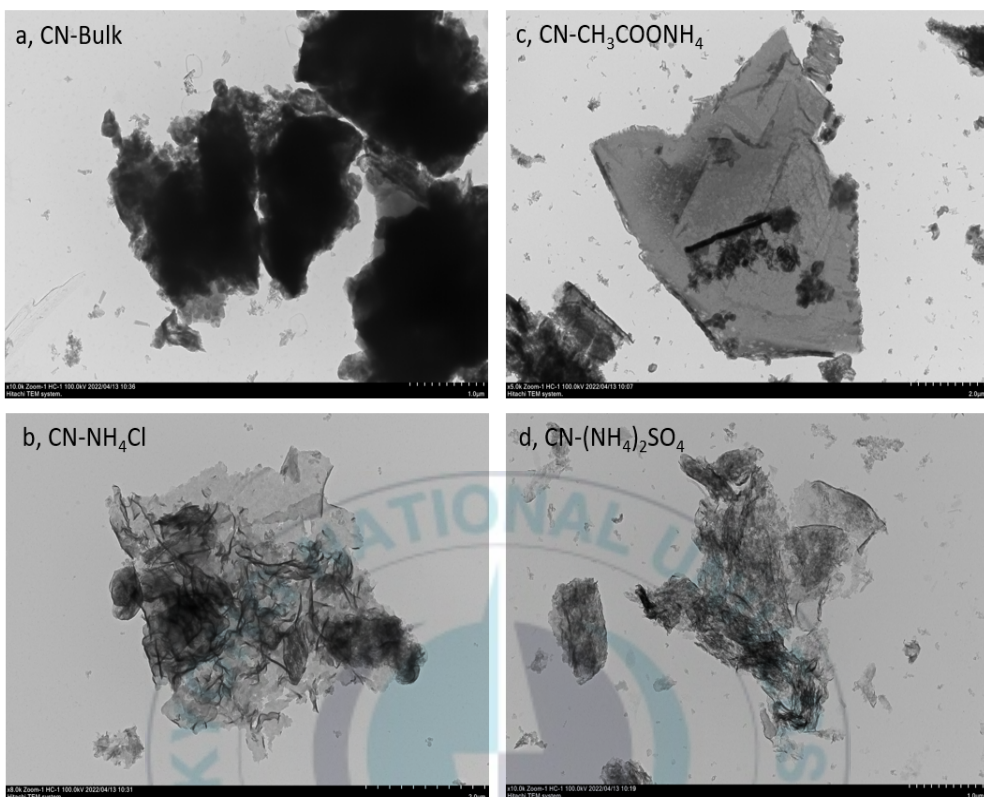


Figure 3.9 TEM images of four samples using different ammonium salts.

XRD pattern was studied to explore the crystalline structure of four as-prepared samples. From the [figure 3.10](#), all samples have two distinct diffraction peaks of g- $C_3N_4$  which are around at location  $13^\circ$  and  $27.6^\circ$  which are referred to the g- $C_3N_4$  diffraction peaks (JCPDS 87-1526) [74]. The plane structural packing pattern and crystal planes of g- $C_3N_4$  correspond to these peaks. It can be obviously seen that the (002) peak of g- $C_3N_4$  modified with ammonium salts have trend to become weaker and quite slightly towards high diffraction angle. The weaker of peak means that the crystallinity of g- $C_3N_4$  decreased than CN-bulk. This change implied to porous nanosheets structure.

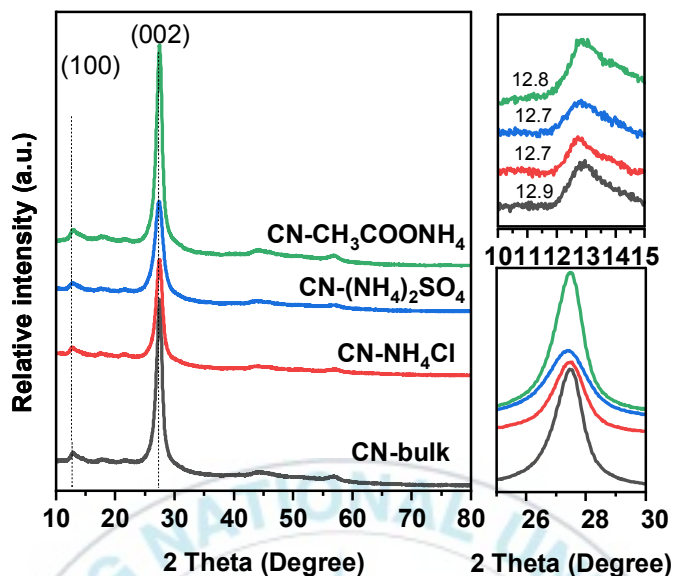


Figure 3.10 XRD pattern of four obtained samples.

The functional group of  $g\text{-C}_3\text{N}_4$  modified with different ammonium salts were detected by FT-IR spectroscopy (Figure 3.11). In the FT-IR spectra, the typical peaks are clear in all four samples. The spectra of all samples were considered in the range  $700\text{-}4000\text{ cm}^{-1}$ . The broad peak between  $3000\text{ to }3500\text{ cm}^{-1}$  is the stretching vibration of N-H and -OH[61]. The strong peaks at  $1200\text{-}1600\text{ cm}^{-1}$  are attributed to the typical tensile vibration mode of C-N heterocycles [62]. The sharp peak at  $800\text{ cm}^{-1}$  represents the vibrational absorption of triazine unit [63]. From above results, the existed functional groups of four as-prepared were confirmed as the  $g\text{-C}_3\text{N}_4$ .

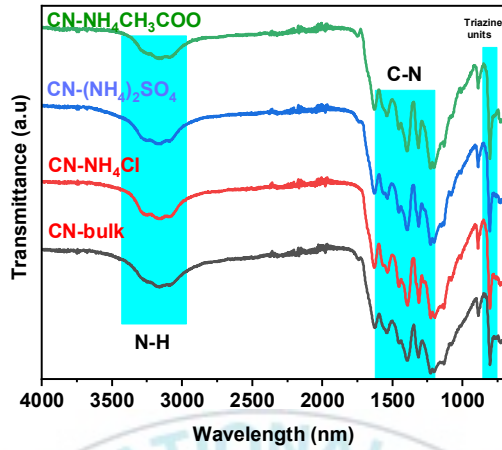


Figure 3.11 FTIR spectra of four samples.

To investigate the optical properties of four samples, UV-vis DRS spectra was measured. The UV-Vis DRS of all samples is shown in figure 3.12. The absorption thresholds of CN-bulk, CN-NH<sub>4</sub>Cl, CN-(NH<sub>4</sub>)<sub>2</sub>SO<sub>4</sub>, and CN-CH<sub>3</sub>COONH<sub>4</sub> were estimated as 472 nm, 463 nm, 456 nm, and 477 nm. This implied that all four samples can absorb visible light. The band-gap transition is responsible for range of absorption light, according to the UV-Vis DRS absorption edges [63]. The optical properties of the photocatalyst can be evaluated using the band gap energy ( $E_g$ ). The Tauc equation can be used to compute  $E_g$  of photocatalysts based on their absorption spectra[65].

$$\alpha h\nu = A (h\nu - E_g)^{n/2} \quad (7)$$

where  $\alpha$ ,  $A$ ,  $h\nu$  and  $E_g$  are the optical absorption coefficient, a proportionality constant, a photo energy, and the band gap energy respectively. The value of  $n$  is determined by the type of optical transition that occurs in semiconductors: direct optical transitions have a value of 1, whereas indirect optical transitions have a value of 4 [66]. Because  $g\text{-C}_3\text{N}_4$  is indirect semiconductor, the value of  $n$  is 4 [67]. The band gaps energy of four as-prepared samples was estimated based on the UV-vis DRS

data. The derived bandgaps from the  $(Ah\nu)^2$  versus photon-energy plots was shown in the figure. The band gap energy of CN-bulk, CN-NH<sub>4</sub>Cl, CN-(NH<sub>4</sub>)<sub>2</sub>SO<sub>4</sub> and CN-CH<sub>3</sub>COONH<sub>4</sub> were estimated as 2.63, 2.72, 2.76 and 2.62 eV (Figure 3.13). Varying band gaps can lead to different band gap levels, which can have a big impact on g-C<sub>3</sub>N<sub>4</sub> samples 's photooxidation and reduction capacities. Even though CN-(NH<sub>4</sub>)<sub>2</sub>SO<sub>4</sub> as a biggest band gap, CN- CN-(NH<sub>4</sub>)<sub>2</sub>SO<sub>4</sub> has a higher redox capability than other samples [39].

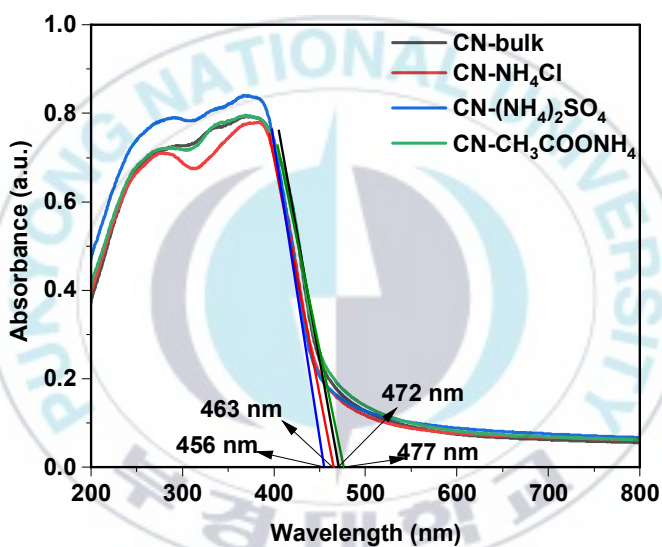


Figure 3.12 UV-visible DRS spectra.

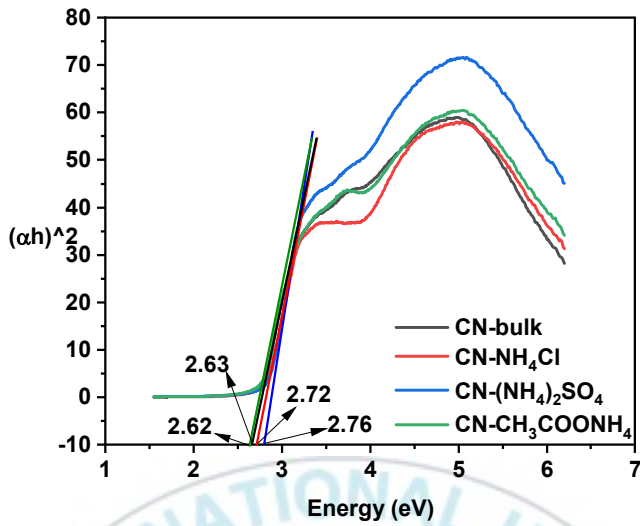


Figure 3.13 Estimated band gap of four as-prepared samples.

PL spectra are used to study the separation and recombination of photogenerated charge carriers. The PL spectra of four samples were excited at wavelength of 360 nm. All the samples have clear PL emission peaks located around 440nm to 460nm (Figure 3.14). Three g-C<sub>3</sub>N<sub>4</sub> samples which modified using ammonium salts have a weaker peak in PL spectra than CN-bulk. This decline of intensity could indicate that charge carrier recombination has been effectively prevented. The reduction in PL intensity can also be attributed to the sample's increased structural flaws and lower crystallinity.

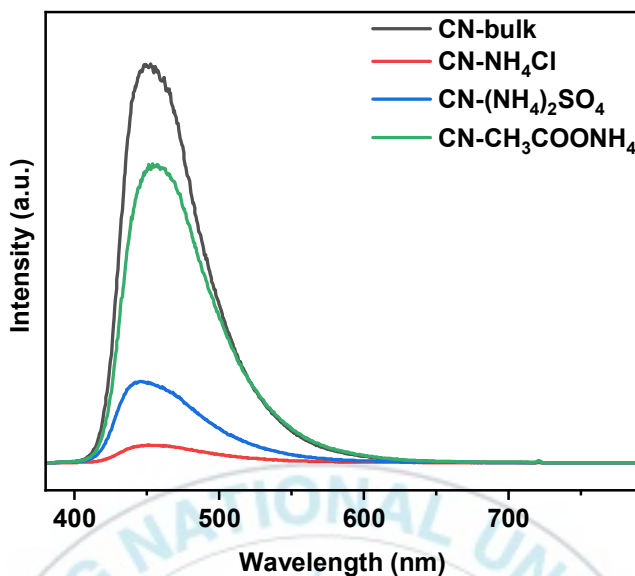


Figure 3.14 PL spectra of four as-prepared samples.

All the samples have a broad PL emission that can be divided into 3 primary Gaussian peaks (Figure 3.15). Three emission peaks at  $P_1$  440 nm,  $P_2$  461 nm, and  $P_3$  499 nm for CN-nanosheets; at  $P_1$  440 nm,  $P_2$  464 nm, and  $P_3$  494 nm for CN-bulk; at  $P_1$  438 nm,  $P_2$  461 nm, and  $P_3$  496 nm for CN-(NH<sub>4</sub>)<sub>2</sub>SO<sub>4</sub>; at  $P_1$  442 nm,  $P_2$  465 nm, and  $P_3$  500 nm for CN which results from the recombination of  $e^-/h^+$  from different pathways in g-C<sub>3</sub>N<sub>4</sub>. The  $sp^2$  C-N  $\pi$  band,  $sp^3$  C-N  $\sigma$  band, and the lone pair state of the bridge N atom transitions contributed these recombination paths come [70].  $P_3$ 's peak position remains approximately 467 nm, owing to the presence of NH<sub>2</sub> on the edge and a defect in C $\equiv$ N [71]. FTIR spectroscopy can be used to further confirm it.

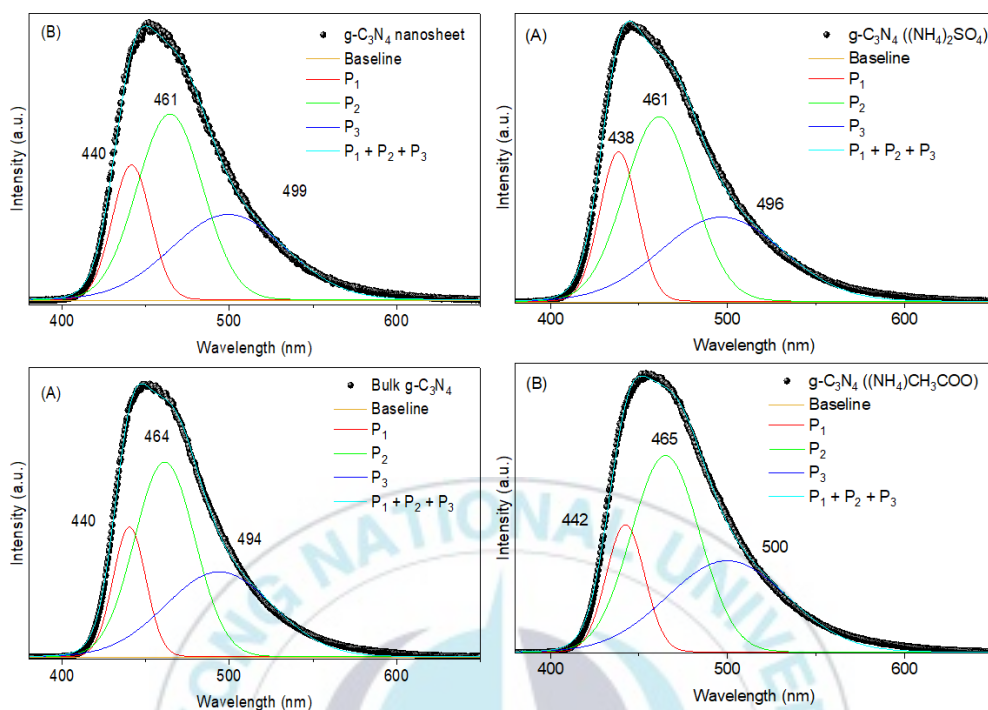


Figure 3.15 Gaussian peak fitting of four samples.

## 3.2 Photocatalytic activity test

### 3.2.1 CN-nanosheets for photodegradation of Rhodamine B under visible light

The photocatalytic efficiency of the CN-nanosheets which was synthesized with ammonium chloride was tested using the experiment of RhB degradation under visible light irradiations. The photocatalytic performance of all samples was shown in the [figure 3.16](#). It can be seen that CN-nanosheets which were made from melamine and ammonium chloride have a higher photocatalytic performance than bulk  $g\text{-C}_3\text{N}_4$ . RhB self-degradation without photocatalyst is almost negligible. After irradiation of 210 min, the degradation efficiency percentage of RhB is approximately 63% and 98% for bulk  $g\text{-C}_3\text{N}_4$  and CN-nanosheets. The results implied that CN-nanosheets have a greater photocatalytic efficiency than bulk  $g\text{-C}_3\text{N}_4$ .

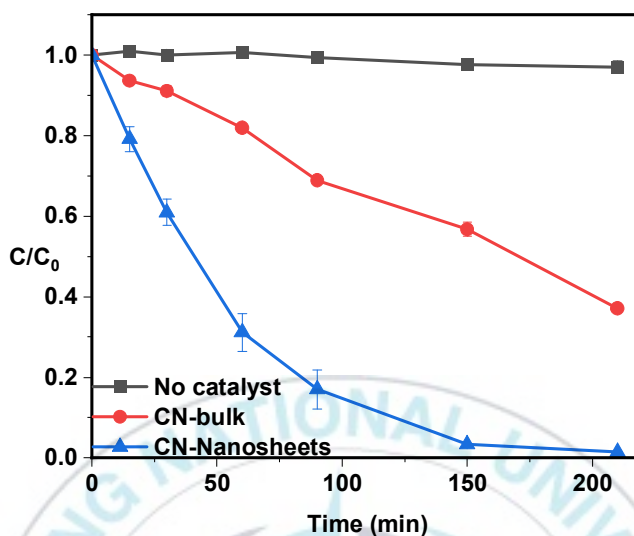


Figure 3.16 Photodegradation rate of RhB under visible light. Condition experimental: [Catalyst] = 0.5 gL<sup>-1</sup>, [RhB] = 20 mgL<sup>-1</sup>, V= 25 mL, Light wavelength > 400 nm.

To investigate the absorption of the dye on the catalyst surface, the experiment was carried out with the same process with photocatalytic activity test without the light irradiation. Firstly, catalysts were dispersed on the RhB solution (20 mgL<sup>-1</sup>) with catalyst dosage 0.5 gL<sup>-1</sup>. The solution was stirring under dark using magnetic stirring and 1 ml samples was taken at interval time (0, 15, 30, 60, 90, 150, and 210 min). From the [figure 3.17](#), the absorption of Rhodamine B on the catalyst surface are negligible and the absorption-desorption equilibrium can be reached after 1hour-stirring.

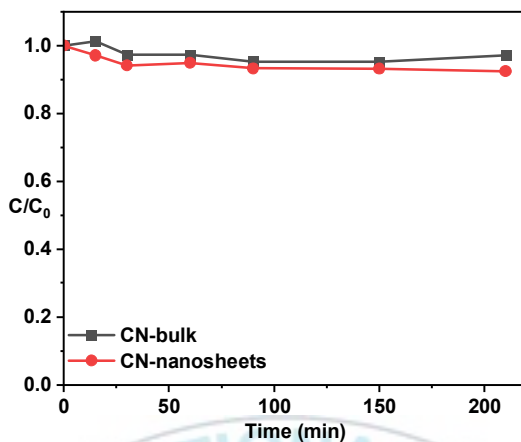


Figure 3.17 The absorption of RhB on the catalyst surface. Condition experimental: [Catalyst] = 0.5 gL<sup>-1</sup>, [RhB] = 20 mgL<sup>-1</sup>, V= 25 mL, In dark.

The UV-vis absorbance spectra also were studied to explore the degree of mineralization of RhB during the photodegradation reaction. It can be found that the absorption peak of RhB changed from 554nm to a shorter wavelength and the strength dropped in CN-nanosheets under visible light (Figure 3.18). With CN-nanosheets, the change is much stronger than CN-bulk, this demonstrated the higher activity of g-C<sub>3</sub>N<sub>4</sub> nanosheet.

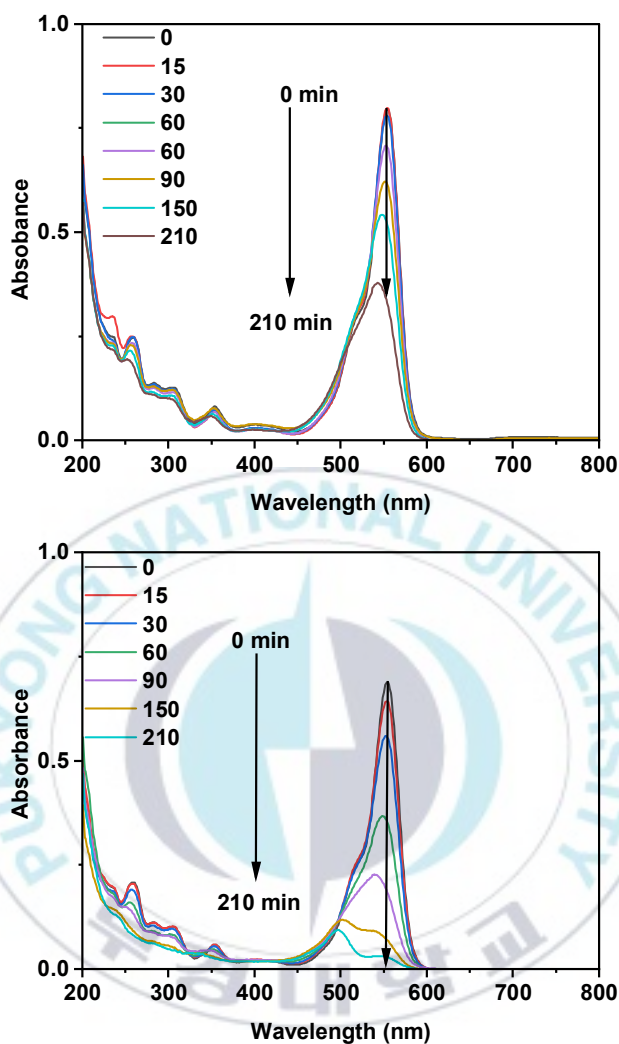


Figure 3.18 The UV-vis spectrum of RhB solution at interval time. Condition experimental: [Catalyst] =  $0.5 \text{ gL}^{-1}$ , [RhB] =  $20 \text{ mgL}^{-1}$ , V= 25 mL, Light wavelength > 400 nm.

The photocatalytic degradation kinetic also was studied using first-order reaction. The rate of change of concentration in a first-order kinetic model is supposed to be proportional to the concentration at a given instant. As a result, for a first-order

photocatalytic degradation with concentration  $C_t$  at time  $t$ , the difference equation is given as

$$\frac{dC_t}{dt} = k \cdot C_t \quad (8)$$

Where  $k$  is called rate constant with the dimension of inverse of time, normally as  $s^{-1}$  [75]. With initial condition  $C_0$  at  $t = 0$ , the solution of differential equation (8) can be written as

$$C_t = C_0 \cdot e^{-kt} \quad (9)$$

To fit first-order kinetic models to experiment data, the least-squares approach is used. When the variables are redefined, linear regression can be simply used to first-order kinetic models. For the kinetic model of first order:

$$-\ln \frac{C_t}{C_0} = k \cdot t \quad (10)$$

When the logarithmic term is utilized as the fitting function, the above equation can be used to fit direct linear regression. The coefficient of determination is a number that indicates how well the regression line approximates the real data points [76]. The  $R^2$  coefficient of determination is defined as

$$R^2 = 1 - \frac{SS_{res}}{SS_{tot}} \quad (11)$$

Where  $SS_{tot}$  is the total sum of squares and  $SS_{res}$  is the sum of squares of residuals:

$$SS_{tot} = \sum_{i=1}^n (y_i - \bar{y})^2, \quad SS_{res} = \sum_{i=1}^n (y_i - f_i)^2 \quad (12)$$

Here,  $n$  is the number of experiments data,  $y_i$  is  $i$ th experimental values,  $\bar{y}$  is the mean experimental values and  $f_i$  stands for  $i$ th modeled value. The value of  $R_2$  is usually between 0 and 1. A high coefficient value indicates that the observations are better suited. The first-order kinetic of two samples for photodecomposition of RhB was shown in the [Figure 3.19](#). The degradation rate constant of CN-nanosheets under visible light irradiation was  $0.0211 \text{ min}^{-1}$ , which is approximately 4.7 times that of

CN-bulk. The photocatalytic oxidation ability of CN-nanosheets is significantly greater than that of CN-bulk, according to the RhB photodegradation experiment. This result is because the CN-nanosheets has greater specific surface area and a longer visible light absorption range compared to CN-bulk.

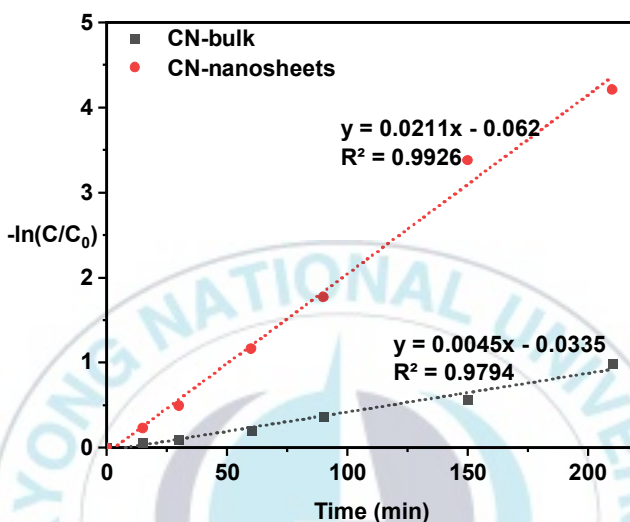


Figure 3.19 First-order kinetic for photodegradation of RhB under visible light. Condition experimental: [Catalyst] = 0.5 gL<sup>-1</sup>, [RhB] = 20 mgL<sup>-1</sup>, V = 25 mL, Light wavelength > 400 nm.

From all above experiments, some parameters of two sample CN-bulk and CN-nanosheets were listed in the table 2. Under visible light, it is obvious that CN-nanosheets produced in the presence of NH<sub>4</sub>Cl have remarkable photocatalytic activity. The significant improvement in photocatalytic oxidation and reduction capacity is explained by the higher separation and transfer efficiency of carrier by CN-nanosheets, as well as the more reactive sites from its structure. CN-nanosheets efficiently eliminated the limits of the g-C<sub>3</sub>N<sub>4</sub>'s recombination rate of photogenerated electrons and hole pair, low specific area, and provides new ways to improve applications.

Table 2: Comparison CN-bulk and CN-nanosheets

Samples	NH <sub>4</sub> Cl	E <sub>g</sub> (eV)	H (%)	k (min <sup>-1</sup> )
CN-bulk	No	2.68	63%	0.0045
CN-nanosheets	Yes	2.78	98%	0.0211

Condition experimental: [Catalyst] = 0.5 gL<sup>-1</sup>, [RhB] = 20 mgL<sup>-1</sup>, V= 25 mL, Light wavelength > 400 nm; E<sub>g</sub>: bandgap energy of catalyst, H: degradation efficiency, and k: degradation rate constant.

The influence of CN-nanosheets dosage on Rhodamine B decomposition was investigated by adjusting the dosage of CN-nanosheets in the photocatalytic reaction from 0.1 to 0.9 g L<sup>-1</sup> in the photocatalytic reaction for 210 min (Figure 3.20). The results show that as the amount of catalyst increase up to 0.9 g L<sup>-1</sup>, the degradation efficiency of Rhodamine B nearly increased up 99%. The number of photon absorption sites increased as the amount of catalyst increased. This led to increase the photodegradation rate of Rhodamine B.

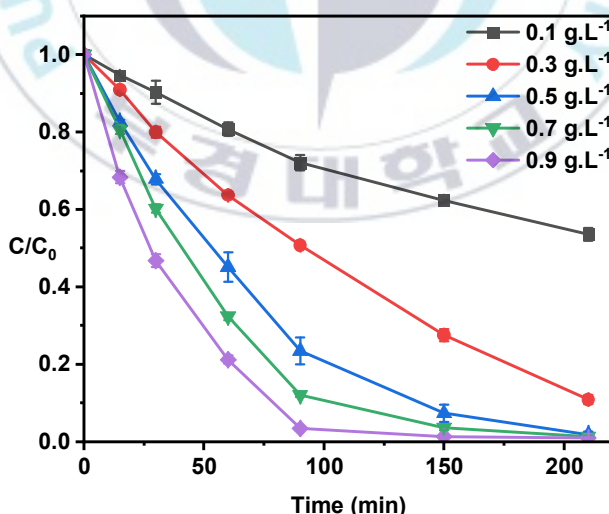


Figure 3.20 Effect of catalyst dosage on photodegradation of Rhodamine B. Condition experimental: [Catalyst] = 0.1 – 0.9 gL<sup>-1</sup>, [RhB] = 20 mgL<sup>-1</sup>, V= 25 mL, Light wavelength > 400 nm.

To find the optimal concentration for CN-nanosheets (using  $0.5 \text{ g L}^{-1}$ ), the effect of initial concentration was evaluated at four different concentrations: 10, 20, 30, and  $40 \text{ mg L}^{-1}$ . The results demonstrate that the percentage of photocatalytic degradation is strongly reliant on the starting concentration of Rhodamine B (Figure 3.21). The percentage of the removal Rhodamine B after 210 min under visible light irradiation were 99.5%, 98.4%, 90.5% and 78.1% for an initial concentration of 10, 20, 30, and  $40 \text{ mg L}^{-1}$  of Rhodamine B, respectively. On the one hand, at lower concentration ( $10 \text{ mg L}^{-1}$ ), the surface catalyst would absorb Rhodamine B molecules and after that, the superoxide radicals ( $\text{O}_2^{\cdot-}$ ) which were formed on the surface catalyst reacted with Rhodamine B molecules. The concentration of Rhodamine B is low thus the number of  $\text{O}_2^{\cdot-}$  generated is enough to effectively degrade dye molecules. On the other hand, the high Rhodamine B concentration could lead to shield of light and finally result in limited production of electron-hole pairs and the number of superoxide radicals. Moreover, at higher concentration, the dye molecules might block the across the catalyst surface, resulting in a decrease in photocatalytic degradation percentage.

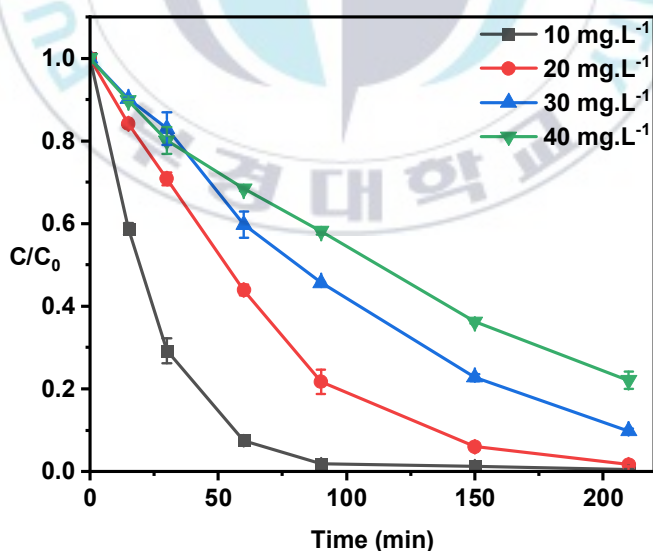


Figure 3.21 Effect of initial concentration of RhB on the photodegradation rate. Condition experimental: [Catalyst] =  $0.5 \text{ g L}^{-1}$ , [RhB] = 10 –  $40 \text{ mg L}^{-1}$ , V= 25 mL, Light wavelength > 400 nm.

The experiment was carried out by adjusting the pH of the dye solution to investigate how it affected the degradation of Rhodamine B. The concentration of Rhodamine B was kept at  $20 \text{ mg L}^{-1}$  and the mass of catalyst is  $0.5 \text{ g L}^{-1}$ . pH was changed with different value: 3, 5, 7, 9 and unadjusted. The figure 3.22 shows the results of degradation percentage for every pH condition. The order of the removal efficiency following  $\text{pH } 3 > \text{pH } 5 > \text{pH } 7 > \text{pH } 9$ .

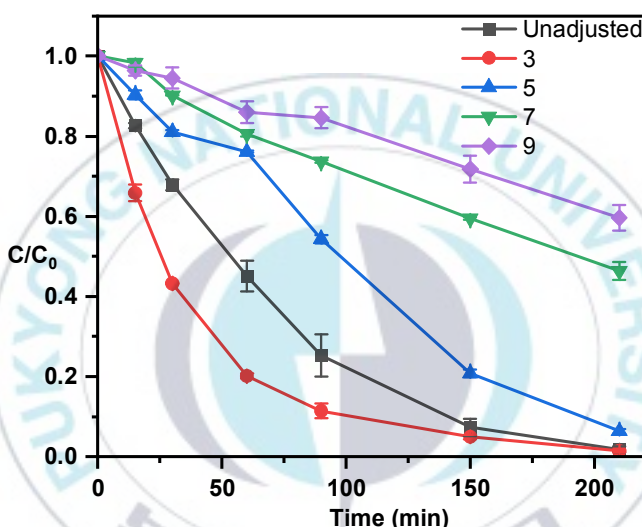


Figure 3.22 Effect of pH on the photodegradation rate of RhB under visible light. Condition experimental:  $[\text{Catalyst}] = 0.5 \text{ g L}^{-1}$ ,  $[\text{RhB}] = 20 \text{ mg L}^{-1}$ ,  $V = 25 \text{ mL}$ , Light wavelength  $> 400 \text{ nm}$ .

The reusability of a catalyst is a significant aspect in its effectiveness in practical applications. In here, the reusability of CN-nanosheets was tested for 4 cycles. After finishing each experiment, the catalyst was centrifuged using high-speed refrigerated centrifuge machine and washed with ethanol and distilled water several times for next experiment. The results are shown in the figure 3.23. The photocatalytic efficiency of the photocatalyst decreased as the cycle was repeated. The removal percentage of Rhodamine B at each cycle were 98%, 95%, 88% and 84%. These results are due to the reduction of the catalyst in the centrifuging and washing process and the

absorption of dye on the catalytic surface. Compared with the first cycle, the removal percentage of Rhodamine B at the second cycle decreased moderately and significantly at the third and fourth cycle.

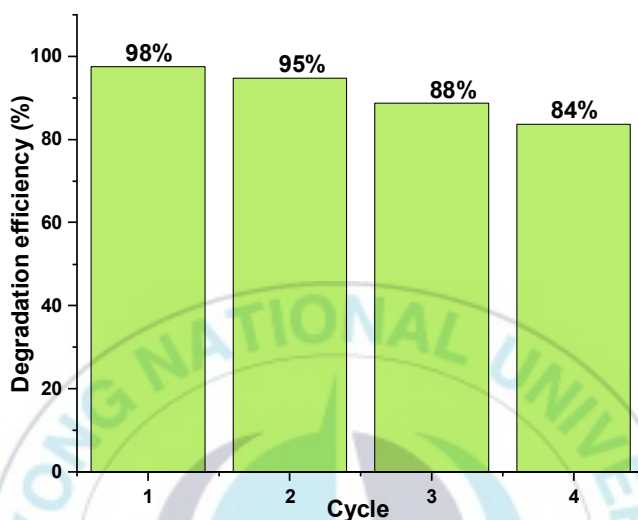


Figure 3.23 Photodegradation rate of CN-nanosheets over 4 cycles. Condition experimental: [Catalyst] =  $0.5 \text{ g L}^{-1}$ , [RhB] =  $20 \text{ mg L}^{-1}$ ,  $V = 25 \text{ mL}$ , Light wavelength  $> 400 \text{ nm}$ .

In addition, the crystalline structure of the CN-nanosheets was also tested by XRD. The crystalline structure before and after the reaction of materials is shown in the [figure 3.24](#). The results of the above analysis show that the crystal structure does not change after the photocatalytic reaction.

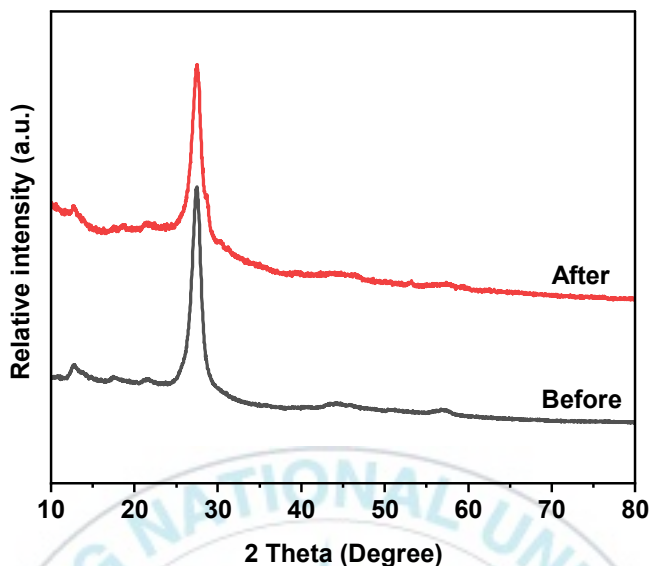


Figure 3.24 The XRD pattern of CN-nanosheets before and after over 4 cycles.

To better understand the mechanism, scavenging experiments were utilized to discover the reactive species in the photocatalytic process. For each scavenger as  $h^+$ ,  $O_2^{\cdot-}$ , and  $OH^{\cdot}$ , triethanolamine (TEA), benzoquinone (BQ) and isopropyl alcohol (IPA) were used. When TEA as  $h^+$  scavengers was added to the mixture, the degradation efficiency of the photocatalyst decreased significantly, as shown in [figure 3.25](#); this change indicated the photogenerated holes have a crucial role in the RhB degradation process. Furthermore, adding BQ to the mixture resulted in a significant decrease in degradation efficiency, demonstrating that the presence of  $O_2^{\cdot-}$  reactive species is critical for the improvement of photocatalytic activity for RhB degradation. Surprisingly, the inclusion of IPA as a scavenger had only a little effect on the degrading efficiency of CN-nanosheets. This result deduced that  $OH^{\cdot}$  was the least active species throughout the photoreaction. To make sure a highly effective for the removal of organic contaminants in wastewater using photocatalytic system, the concentration of scavenging chemicals such as TEA (amine-based) and IPA

(hydroxyl-based) should be significantly reduced through physical or biological pretreatment.

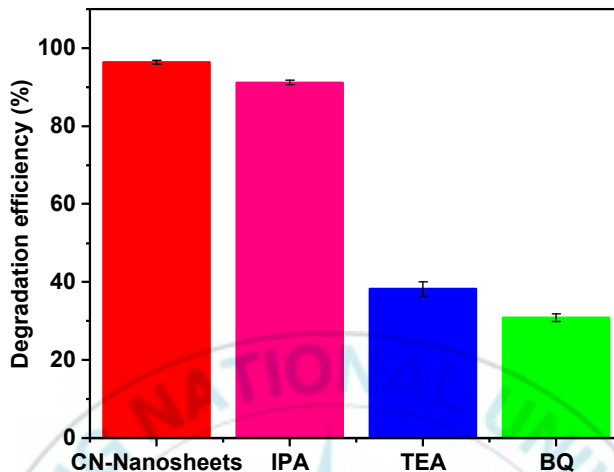
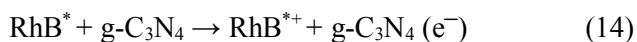


Figure 3.25 Active species trapping experiments of CN-nanosheets in degradation. RhB. Condition experimental: [Catalyst] =  $0.5 \text{ gL}^{-1}$ , [RhB] =  $20 \text{ mgL}^{-1}$ ,  $V = 25 \text{ mL}$ , Light wavelength  $> 400 \text{ nm}$ .

The following is a detailed discussion of the likely predicted mechanism for improved RhB degradation utilizing CN-nanosheets catalyst under visible light exposure. The self-photo dye sensitization process is Pathway 1. In this process, the RhB molecules absorb visible light and undergo their own oxidative transformation, resulting in the direct creation of oxidizing OH radicals. RhB releases an electron from its valence band to the conduction band under light irradiation, leaving RhB in an excited state (RhB\*) that can be singlet or triplet. This causes the photoinduced electron to be injected into the CN-nanosheets' conduction band, where RhB\* is transformed to the radical cation RhB<sup>\*+</sup>. As a result, RhB acts as a photosensitizer. The RhB<sup>\*+</sup> radical was degraded itself or by the formed reactive oxygen species. The conduction band of CN-nanosheets is only used as an electron acceptor level in this process, while the

valence band is left unused. The reaction pathways' mechanism is depicted in the below equations:



Pathway 2 of the degradation RhB is semiconductor mediated photodegradation process. A photocatalysis mechanism is proposed and shown in the [figure 3.26](#). To begin, visible light is used to excite electrons from the VB to the CB of g-C<sub>3</sub>N<sub>4</sub>, leaving holes on the VB. The electron-hole pairs are then generated and used in the oxidation and reduction processes. The superoxide radical O<sub>2</sub><sup>•-</sup> and h<sup>+</sup> produced during the reduction process interact with the organic pollutant Rhodamine B to convert it to the non-toxic compound's H<sub>2</sub>O and CO<sub>2</sub>.



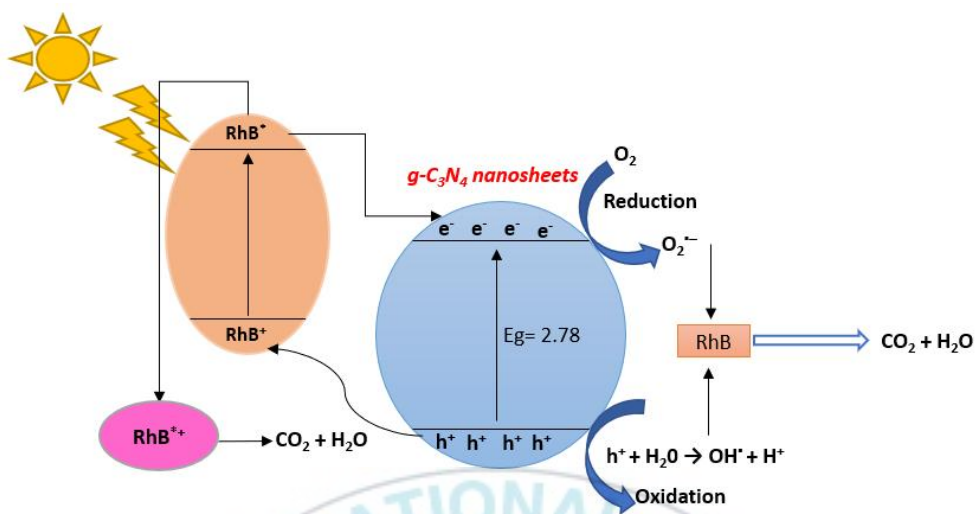


Figure 3.26 The proposed mechanism for degradation of RhB using g-C<sub>3</sub>N<sub>4</sub> nanosheets when exposed under visible light exposure.

### 3.2.2 g-C<sub>3</sub>N<sub>4</sub> modified using different ammonium salts

The photocatalytic efficiency of four samples was studied by the photodecomposition RhB test. Figure 3.27 shows the photocatalytic performance of four different as-prepared samples under visible light ( $\geq 400$  nm). CN-(NH<sub>4</sub>)<sub>2</sub>SO<sub>4</sub> which was synthesized from melamine and ammonium sulfate has highest activity with the removal percentage 99% after 210 min. The g-C<sub>3</sub>N<sub>4</sub> synthesized from melamine and ammonium chloride also shown excellent performance with 98% of Rhodamine B removal while the removal percentage are only 67% and 63% with g-C<sub>3</sub>N<sub>4</sub> from melamine and ammonium acetate and CN-bulk. This implied that synthesizing g-C<sub>3</sub>N<sub>4</sub> with ammonium salts can increase its photocatalytic activity.

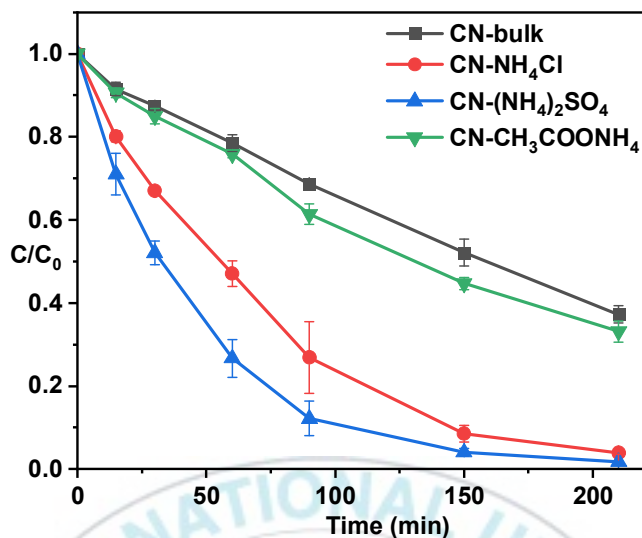


Figure 3.27 Photodegradation rate of Rhodamine B using four as-prepared samples under visible light. Condition experimental: [Catalyst] =  $0.5 \text{ g L}^{-1}$ , [RhB] =  $20 \text{ mg L}^{-1}$ ,  $V = 25 \text{ mL}$ , Light wavelength  $> 400 \text{ nm}$ .

To investigate the absorption of the dye on the catalyst surface, the experiment was carried out with the same process with photocatalytic activity test without the light irradiation. Firstly, catalysts were dispersed on the Rhodamine B solution ( $20 \text{ mg L}^{-1}$ ) with catalyst dosage  $0.5 \text{ g L}^{-1}$ . The solution was stirring under dark using magnetic stirring and 1 ml samples was taken at interval time (0, 15, 30, 60, 90, 150, and 210 min). From the [figure 3.28](#), the absorption of Rhodamine B on the catalyst surface are negligible and the absorption-desorption equilibrium can be reached after stirring 1 hour.

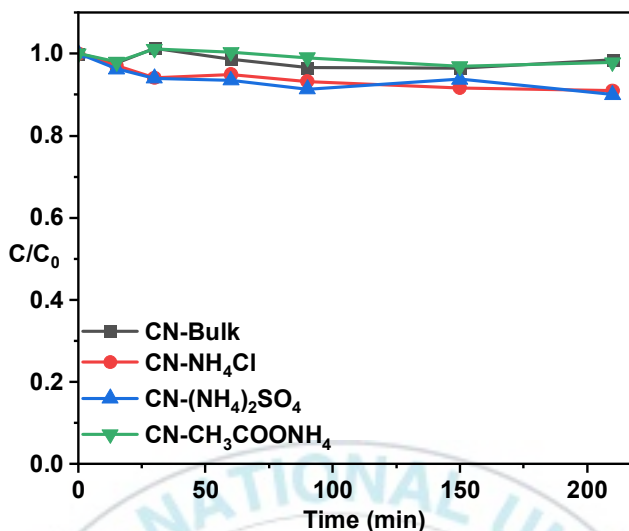


Figure 2 Absorption of Rhodamine B on the catalyst surface Condition experimental: [Catalyst] =  $0.5 \text{ gL}^{-1}$ , [RhB] =  $20 \text{ mg L}^{-1}$ , V = 25 mL, In Dark.

The UV-vis absorbance spectra of four samples were also presented to illustrate the rate of degradation of Rhodamine B (figure 3.29). The absorption peak of Rhodamine B moved from 554 nm to a shorter wavelength under visible light irradiation, and the intensity decreased. These changes imply that the ethyl group in RhB has been eliminated. Finally, the absorption peak dropped, suggesting the destruction of RhB's benzene ring [77]. As the results of the removal percentage, the change in CN-(NH<sub>4</sub>)<sub>2</sub>SO<sub>4</sub> has greatest, following CN-NH<sub>4</sub>Cl, CN-CH<sub>3</sub>COONH<sub>4</sub> and CN-bulk.

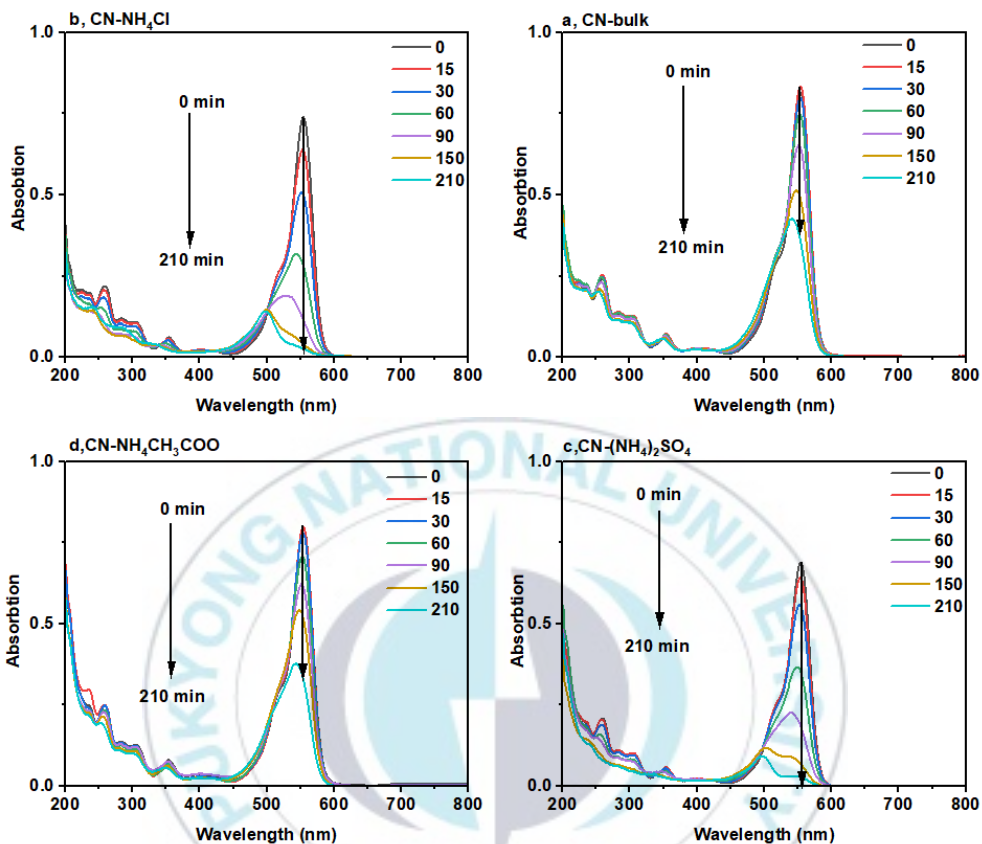


Figure 3.29 The UV-vis spectrum of Rhodamine B solution at interval time. Condition experimental: [Catalyst] = 0.5 gL<sup>-1</sup>, [RhB] = 20 mgL<sup>-1</sup>, V= 25 mL, Light wavelength > 400 nm.

The photocatalytic degradation kinetic also was studied. The rate of change of concentration in a first-order kinetic model is supposed to be proportional to the concentration at a given instant. For the first-order kinetic model, the decay of RhB can be written as

$$-\ln \frac{C_t}{C_0} = k \cdot t \quad (20)$$

Where  $k$  is rate constant with the dimension of inverse of time (s<sup>-1</sup>),  $C_0$ : initial concentration of RhB, and  $C_t$ : concentration of RhB at time  $t$ . Under visible light

irradiation, the degradation rate constant of CN-(NH<sub>4</sub>)<sub>2</sub>SO<sub>4</sub> is highest with 0.0197 min<sup>-1</sup>, which is approximately 1.3 times that of CN-(NH<sub>4</sub>Cl), 3.71 times that of CN-CH<sub>3</sub>COONH<sub>4</sub> and 4.3 times that of CN-bulk (figure 3.30). The photocatalytic degradation RhB confirms that the photocatalytic oxidation ability of CN-(NH<sub>4</sub>)<sub>2</sub>SO<sub>4</sub> is highest. All g-C<sub>3</sub>N<sub>4</sub> samples synthesized in the presence of ammonium salts exhibited a higher degradation rate of RhB than g-C<sub>3</sub>N<sub>4</sub> bulk.

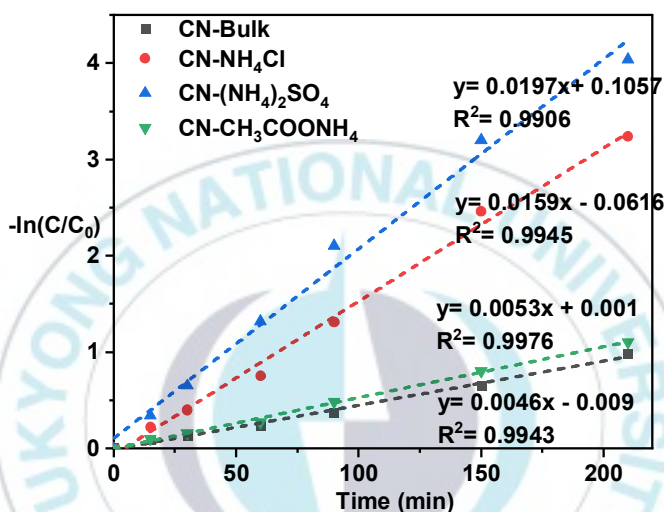


Figure 3.30 First-order kinetic curves for photodegradation of Rhodamine B under visible light. Condition experimental: [Catalyst] = 0.5 gL<sup>-1</sup>, [RhB] = 20 mgL<sup>-1</sup>, V = 25 mL, Light wavelength > 400 nm.

From all above experiments, some parameters of four sample CN-bulk, CN-NH<sub>4</sub>Cl, CN-(NH<sub>4</sub>)<sub>2</sub>SO<sub>4</sub>, and CN-CH<sub>3</sub>COONH<sub>4</sub> were listed in the table 3. It can be clearly observed that all g-C<sub>3</sub>N<sub>4</sub> samples which was synthesized in the presence of ammonium salts (NH<sub>4</sub>Cl, (NH<sub>4</sub>)<sub>2</sub>SO<sub>4</sub>, and NH<sub>4</sub>CH<sub>3</sub>COO) have exhibited more excellent photocatalytic efficiency than g-C<sub>3</sub>N<sub>4</sub> bulk under visible light. The increased separation and transfer efficiency of carrier and the more reactive site from its structure results to the significant improvement of photocatalytic oxidation and reduction ability. In the synthesis process, ammonium salts in high temperature generated some dynamic gases such NH<sub>3</sub>, HCl, SO<sub>4</sub>, H<sub>2</sub>O which destroyed g-C<sub>3</sub>N<sub>4</sub>

bulk into small molecules. This change effectively solved the limitations of CN-bulk as the high recombination rate of photogenerated electrons a hole pair and low specific area.

Table 3 Comparison of four as-prepared samples

Sample	Ammonium salts	$E_g$ (eV)	H (%)	k ( $\text{min}^{-1}$ )
CN-bulk	No	2.63	63 %	0.0046
CN-NH <sub>4</sub> Cl	NH <sub>4</sub> Cl	2.72	98 %	0.0159
CN-(NH <sub>4</sub> ) <sub>2</sub> SO <sub>4</sub>	(NH <sub>4</sub> ) <sub>2</sub> SO <sub>4</sub>	2.76	99 %	0.0197
CN-CH <sub>3</sub> COONH <sub>4</sub>	CH <sub>3</sub> COONH <sub>4</sub>	2.62	67 %	0.0053

Condition experimental: [Catalyst] = 0.5  $\text{g L}^{-1}$ , [RhB] = 20  $\text{mg L}^{-1}$ , V= 25 mL, Light wavelength > 400 nm;  $E_g$ : bandgap energy of catalyst, H: degradation efficiency, and k: degradant rate constant.

The influence of pH, catalyst dosage, and dye initial concentration in the photocatalytic reaction was investigated using CN-(NH<sub>4</sub>)<sub>2</sub>SO<sub>4</sub> as objective. The impact of catalyst dosage on the degradation of RhB (20  $\text{mg L}^{-1}$ ) was checked by varying the concentration of CN-(NH<sub>4</sub>)<sub>2</sub>SO<sub>4</sub> from 0.1 to 0.9  $\text{g L}^{-1}$  in the photocatalytic reaction for 210 min (figure 3.31). With the amount of catalyst increase up to 0.9  $\text{g L}^{-1}$ , it takes only about 60 min to removal more than 90% of Rhodamine B. While the removal efficiency was about 50% after 210 min with 0.1  $\text{g L}^{-1}$  of catalyst. When the amount of catalyst increased, the number of photon absorption sites also grew up. This made the photodegradation of Rhodamine B took place faster.

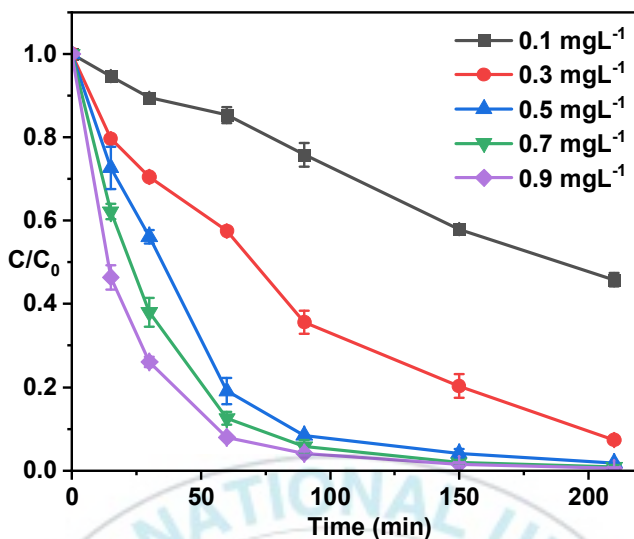


Figure 3.31 Effect of  $\text{CN}-(\text{NH}_4)_2\text{SO}_4$  dosage on the photodegradation rate of RhB. Condition experimental:  $[\text{Catalyst}] = 0.1 - 0.9 \text{ g L}^{-1}$ ,  $[\text{RhB}] = 20 \text{ mg L}^{-1}$ ,  $V = 25 \text{ mL}$ , Light wavelength  $> 400 \text{ nm}$ .

To explore the influence of initial concentration of dye, the photodegradation of RhB using  $\text{CN}-(\text{NH}_4)_2\text{SO}_4$  (dosage:  $0.5 \text{ g L}^{-1}$ ) was carried out at four different initial dye concentrations: 10, 20, 30, 40  $\text{mg L}^{-1}$  (figure 3.32). The figure shows that the initial concentration of dye has significant impact to the removal percentage of Rhodamine B. The removal percentage after 210 min under visible irradiations were 99.5%, 99%, 95.5%, and 89.9% for initial concentration of 10, 20, 30, and 40  $\text{mg L}^{-1}$  of Rhodamine B. On the one hand, at lower concentrations ( $10 \text{ mg L}^{-1}$ ), the surface catalyst would absorb Rhodamine B molecules and then react with Rhodamine B molecules via the superoxide radical ( $\text{O}_2^{\cdot-}$ ) generated on the surface catalyst. Because the concentration of Rhodamine B is low, the amount of superoxide radical produced is sufficient to destroy dye molecules effectively. On the other hand, a high Rhodamine B concentration could cause a light shield, limiting electron-hole pair generation and the quantity of hydroxyl radicals produced. Furthermore, at larger concentrations, the

dye molecules might block the across the catalyst surface, resulting in a decrease in photocatalytic degradation percentage.

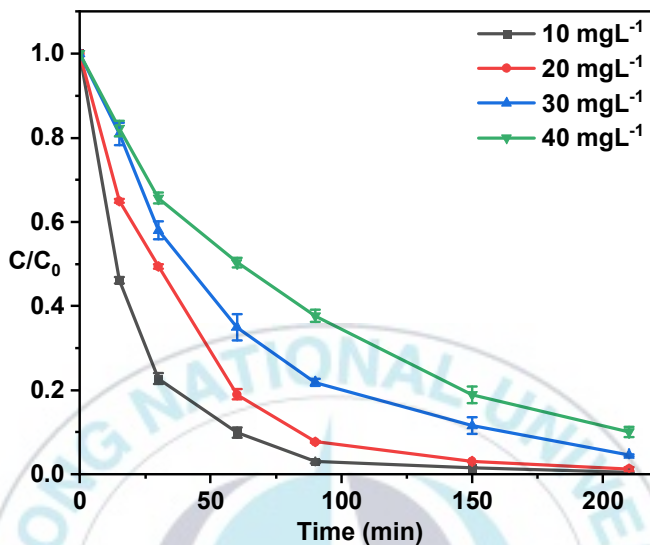


Figure 3.32 Effect of initial concentration Rhodamine B for photodegradation rate under visible light. Condition experimental: [Catalyst] = 0.5 gL<sup>-1</sup>, [RhB] = 20 mgL<sup>-1</sup>, V= 25 mL, Light wavelength > 400 nm.

The experiment was carried out by adjusting the pH of the dye solution to evaluate the influence of starting pH on Rhodamine B degradation. The Rhodamine B concentration was fixed at 20 mg L<sup>-1</sup>, and the catalyst mass was 0.5g L<sup>-1</sup>. Different pH values were used in the experiments as 3, 5, 7, 9, and unadjusted. The figure 3.33 show the percentage of degradation for each pH condition. Following pH 3 > pH 5 > pH 7 > pH 9, the order of removal efficiency is pH 3 > pH 5 > pH 7 > pH 9.

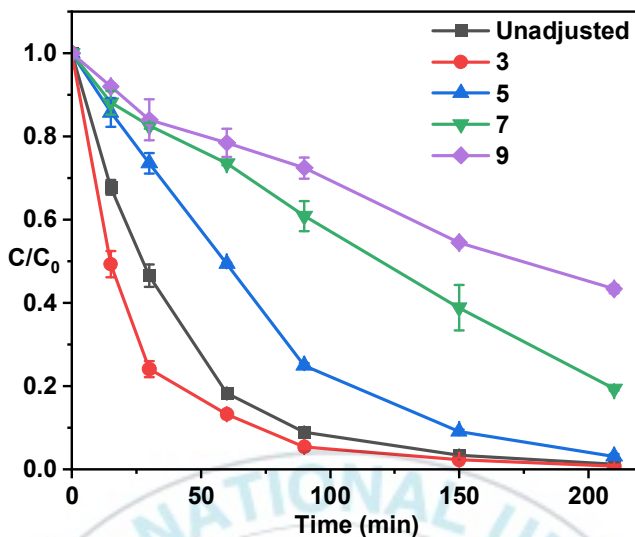


Figure 3.33 Effect of pH on photodegradation of Rhodamine B. Condition experimental: [Catalyst] = 0.5 gL<sup>-1</sup>, [RhB] = 20 mgL<sup>-1</sup>, V= 25 mL, Light wavelength > 400 nm.

The reusability of a catalyst is a crucial factor in its applicability in application areas. The reusability of CN-(NH<sub>4</sub>)<sub>2</sub>SO<sub>4</sub> was investigated for four cycles in this study (figure 3.34). After each experiment, the catalyst was centrifuged using high-speed refrigerated centrifuge machine and washed many times with ethanol and distilled water before moving on to the next cycle. The results are depicted in the figure. The photocatalytic activity of the material declined as the cycle was repeated, as can be shown. Each cycle had a removal percentage of Rhodamine B of 99.5%, 96.5%, 89.2% and 86.4%. This is due to the catalyst being reduced during the centrifuging and washing processes, as well as dye absorption on the catalytic surface.

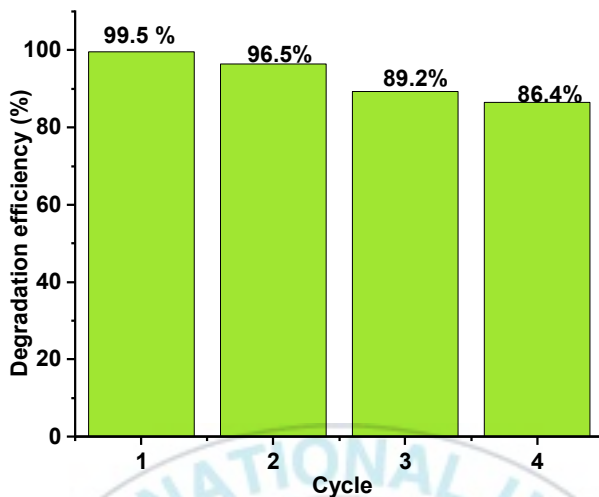


Figure 3 Photodegradation rate of Rhodamine B over 4 cycles using CN-(NH<sub>4</sub>)<sub>2</sub>SO<sub>4</sub>. Condition experimental: [Catalyst] = 0.5 gL<sup>-1</sup>, [RhB] = 20 mgL<sup>-1</sup>, V= 25 mL, Light wavelength > 400 nm.

XRD was also used to evaluate the crystalline structure of the CN-(NH<sub>4</sub>)<sub>2</sub>SO<sub>4</sub>. The [figure 3.35](#) exhibits the crystalline structure before and after the reaction of materials. The results of the following analysis show that after the photocatalytic reaction, the crystal structure does not change.

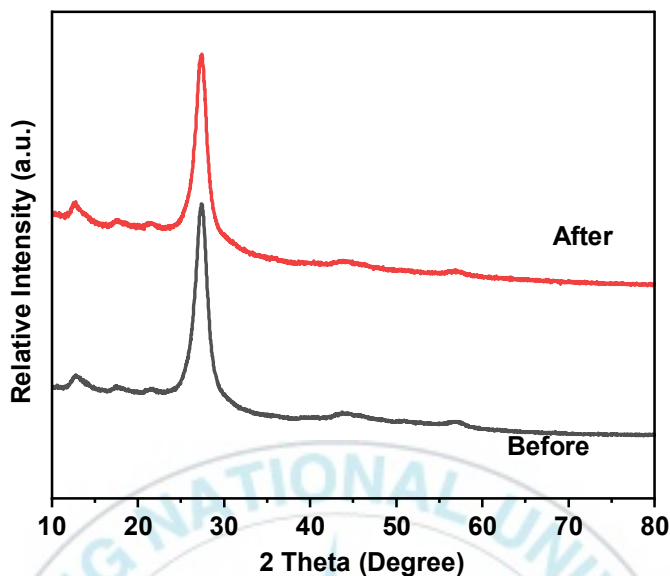


Figure 3.35 XRD pattern of CN-(NH<sub>4</sub>)<sub>2</sub>SO<sub>4</sub> before and after over 4 cycles

To further understand the mechanism of photocatalysis, scavenging experiments were utilized to identify reactive species in the process. As  $h^+$ ,  $O_2^{\cdot-}$ , and  $OH^{\cdot}$  scavengers, triethanolamine (TEA), benzoquinone (BQ), and isopropyl alcohol (IPA) were used. When TEA as  $h^+$  scavengers and BQ as  $O_2^{\cdot-}$  were added to the mixture, the degrading efficiency of the photocatalyst decreased significantly, as shown in figure 3.36. This meant that the reactive species  $h^+$  and  $O_2^{\cdot-}$  played a key role in increasing photocatalytic activity for Rhodamine B degradation. When IPA was introduced as a scavenger, however, there was only a little influence on the degrading efficiency of CN-nanosheets. The results showed that during the photoreaction,  $OH^{\cdot}$  was the lowest active species. To make sure a highly effective photocatalytic system in the removal of surface organic contaminants, the presence of scavenging chemicals such as TEA (amine-based) and IPA (hydroxyl-based) in wastewater treatment systems should be minimized through physical or biological purification processes.

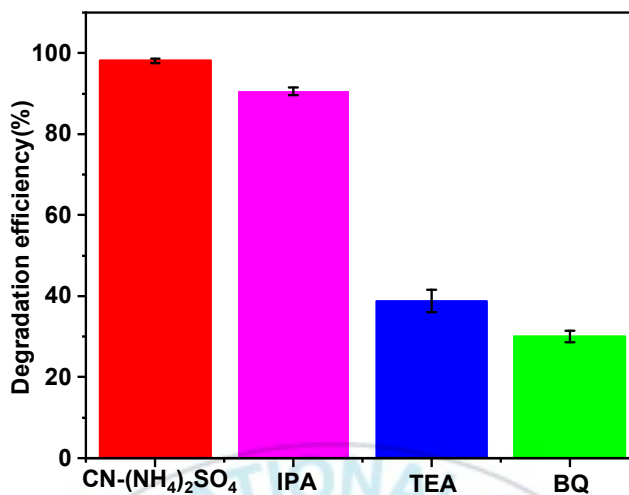
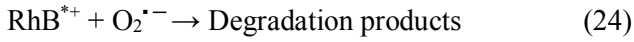
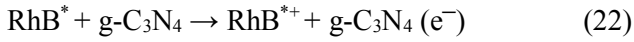
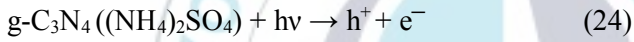


Figure 3.36 Active species trapping experiments of CN-(NH<sub>4</sub>)<sub>2</sub>SO<sub>4</sub> in degradation Rhodamine B. Condition experimental: [Catalyst] = 0.5 gL<sup>-1</sup>, [RhB] = 20 mgL<sup>-1</sup>, V= 25 mL, Light wavelength > 400 nm.

On the basis, the possible expected pathway to photodegradation of RhB using CN-(NH<sub>4</sub>)<sub>2</sub>SO<sub>4</sub> catalyst are the same with the mechanism of degradation of RhB using CN-nanosheets under visible light which were discussed in detail above. Pathway 1 is the process of self-photo dye sensitization. The RhB molecules absorb visible light and undergo their own oxidative transformation, resulting in the direct generation of oxidizing radicals in this photosensitization process. RhB releases an electron from its valence band to the conduction band under light irradiation, leaving RhB in an excited state (RhB\*) that can be singlet or triplet. This causes the photoinduced electron to be injected into the CN-(NH<sub>4</sub>)<sub>2</sub>SO<sub>4</sub> conduction band, where RhB\* is now transformed to the radical cation RhB<sup>\*+</sup>. As a result, RhB acts as a photosensitizer. The RhB<sup>\*+</sup> radical was degraded either by itself or by the reactive oxygen species that generated. The conduction band of CN-(NH<sub>4</sub>)<sub>2</sub>SO<sub>4</sub> is reduced to an electron acceptor level in this method, while the valence band is neglected. The reaction pathways' mechanism is depicted in the diagram below.



Pathway 2 of the degradation RhB is semiconductor mediated photodegradation process. A photocatalysis mechanism is proposed and shown in the [figure 3.37](#). To begin, visible light is used to excite electrons from the VB to the CB of g-C<sub>3</sub>N<sub>4</sub>, leaving holes on the VB. The electron-hole pairs are then generated and used in the oxidation and reduction processes. The superoxide radical O<sub>2</sub><sup>•-</sup> and h<sup>+</sup> produced during the reduction process interact with the organic pollutant Rhodamine B to convert it to the non-toxic compound's H<sub>2</sub>O and CO<sub>2</sub>.



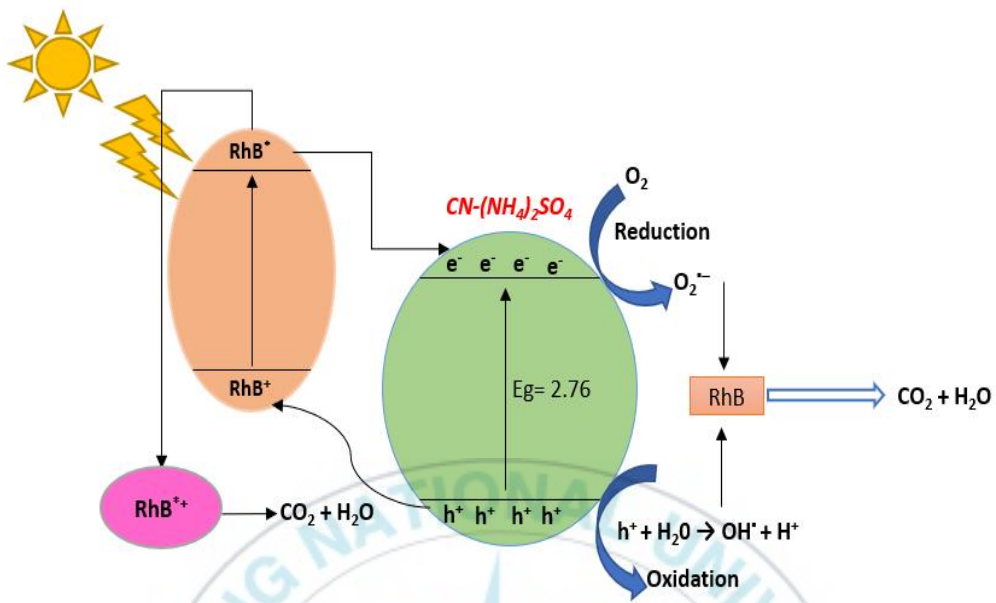


Figure 3.37 The proposed mechanism for degradation of RhB using  $CN-(NH_4)_2SO_4$  when exposed under visible light exposure

## CHAPTER 4: CONCLUSION

In this thesis, we synthesized g-C<sub>3</sub>N<sub>4</sub> using melamine and different ammonium salts to degrade organic dye under visible light. Some conclusions can be summarized as following:

- (1) Successfully prepared g-C<sub>3</sub>N<sub>4</sub> nanosheets by one-step pyrolysis process of melamine and ammonium chloride.
- (2) NH<sub>4</sub>Cl was used as a dynamic gas template in solid-state processes which help to form nanosheets structure of g-C<sub>3</sub>N<sub>4</sub>.
- (3) The degradation efficiency of g-C<sub>3</sub>N<sub>4</sub> nanosheets is approximately 98% after 210 min which significantly increased to compare to 63% of g-C<sub>3</sub>N<sub>4</sub> bulk.
- (4) Ammonium salts-assisted polycondensation for g-C<sub>3</sub>N<sub>4</sub> have been developed. In polymerization process, NH<sub>4</sub>Cl, (NH<sub>4</sub>)<sub>2</sub>SO<sub>4</sub>, CH<sub>3</sub>COONH<sub>4</sub> as a dynamic gas template to support the creation of a thin and porous g-C<sub>3</sub>N<sub>4</sub>.
- (5) The order of the degradation efficiency is following CN-(NH<sub>4</sub>)<sub>2</sub>SO<sub>4</sub> > CN-NH<sub>4</sub>Cl > CN-NH<sub>4</sub>CH<sub>3</sub>COO > CN-bulk (99%, 98%, 67%, 63%).
- (6) The effect of catalyst dosage, pH, concentration of RhB on the degradation efficiency using g-C<sub>3</sub>N<sub>4</sub> nanosheets was also investigated.
- (7) h<sup>+</sup> and <sup>•</sup>O<sub>2</sub><sup>-</sup> species were demonstrated as the critical reactive species for the RhB.

## APPENDIX

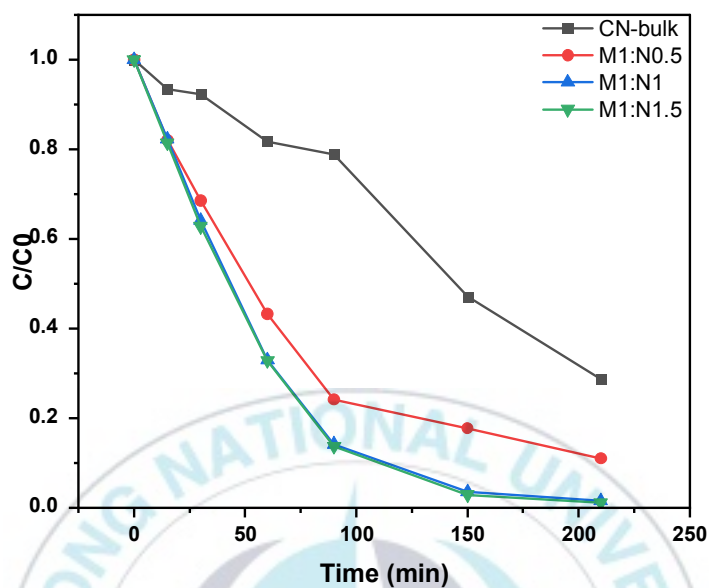


Figure A1: Photodegradation rate of RhB with different ratio of ammonium chloride

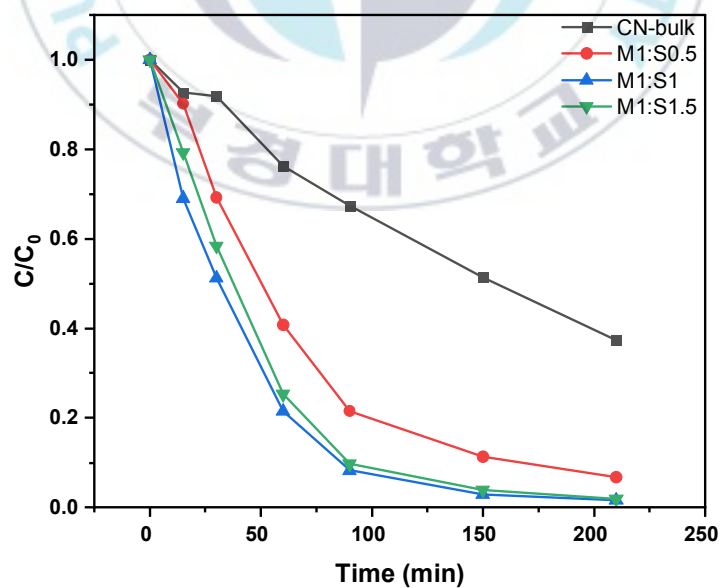


Figure A2: Photodegradation rate of RhB with different ratio of ammonium sulfate

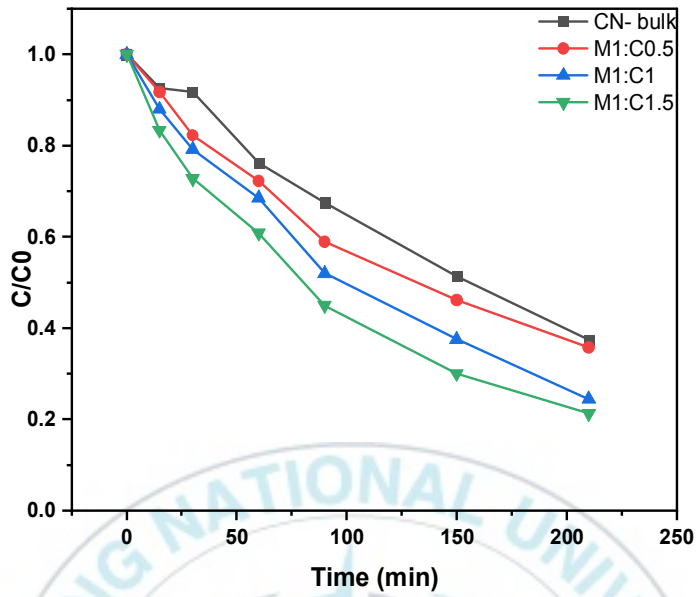
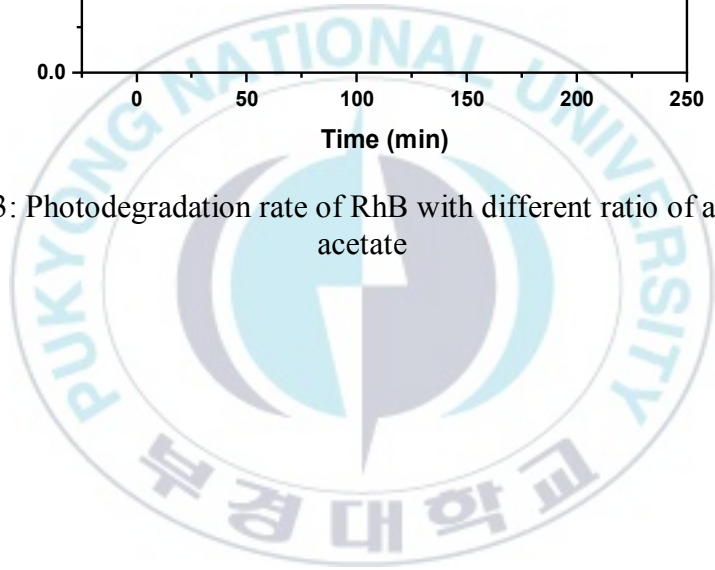


Figure A3: Photodegradation rate of RhB with different ratio of ammonium acetate



## REFERENCES

- [1] Z. Bian, T. Tachikawa, P. Zhang, M. Fujitsuka, and T. Majima, "Au/TiO<sub>2</sub> superstructure-based plasmonic photocatalysts exhibiting efficient charge separation and unprecedented activity," *J Am Chem Soc*, vol. 136, no. 1, pp. 458–465, Jan. 2014, doi: 10.1021/ja410994f.
- [2] K. Honda, "One and Two-dimensional Structure of Alpha-Helix and Beta-Sheet Forms of Poly(L-Alanine) shown by Specific Heat Measurements at Low Temperatures (1.5-20 K)," 1910.
- [3] S. Zhu and D. Wang, "Photocatalysis: Basic principles, diverse forms of implementations and emerging scientific opportunities," *Advanced Energy Materials*, vol. 7, no. 23. Wiley-VCH Verlag, Dec. 06, 2017. doi: 10.1002/aenm.201700841.
- [4] F. Zhang *et al.*, "Recent advances and applications of semiconductor photocatalytic technology," *Applied Sciences (Switzerland)*, vol. 9, no. 12. MDPI AG, Jun. 01, 2019. doi: 10.3390/app9122489.
- [5] M. Dozzi and E. Selli, "Surface Aspects of Semiconductor Photochemistry," *Surfaces*, vol. 3, no. 3, pp. 467–472, Sep. 2020, doi: 10.3390/surfaces3030033.
- [6] Y. Guo, H. Li, W. Ma, W. Shi, Y. Zhu, and W. Choi, "Photocatalytic activity enhanced via surface hybridization," *Carbon Energy*, vol. 2, no. 3. Blackwell Publishing Inc., pp. 308–349, Sep. 01, 2020. doi: 10.1002/cey2.66.
- [7] K. T. Amakiri, A. Angelis-Dimakis, and A. R. Canon, "Recent advances, influencing factors, and future research prospects using photocatalytic process for produced water treatment," *Water Science and Technology*, vol. 85, no. 3, pp. 769–788, Feb. 2022, doi: 10.2166/wst.2021.641.
- [8] H. M. Coleman, V. Vimonses, G. Leslie, and R. Amal, "Degradation of 1,4-dioxane in water using TiO<sub>2</sub> based photocatalytic and H<sub>2</sub>O<sub>2</sub>/UV processes," *Journal of Hazardous Materials*, vol. 146, no. 3, pp. 496–501, Jul. 2007, doi: 10.1016/j.jhazmat.2007.04.049.
- [9] R. A. Putri, S. Safni, N. Jamarun, U. Septiani, M. K. Kim, and K. D. Zoh, "Degradation and mineralization of violet-3B dye using C-N-codoped TiO<sub>2</sub> photocatalyst," *Environmental Engineering Research*, vol. 25, no. 4, pp. 529–535, Aug. 2020, doi: 10.4491/eer.2019.196.

- [10] B. K. Shukla, S. Rawat, M. K. Gautam, H. Bhandari, S. Garg, and J. Singh, "Photocatalytic Degradation of Orange G Dye by Using Bismuth Molybdate: Photocatalysis Optimization and Modeling via Definitive Screening Designs," *Molecules*, vol. 27, no. 7, p. 2309, Apr. 2022, doi: 10.3390/molecules27072309.
- [11] M. N. Chong, B. Jin, H. Y. Zhu, C. W. K. Chow, and C. Saint, "Application of H-titanate nanofibers for degradation of Congo Red in an annular slurry photoreactor," *Chemical Engineering Journal*, vol. 150, no. 1, pp. 49–54, Jul. 2009, doi: 10.1016/j.cej.2008.12.002.
- [12] T. Mahmood, M. T. Saddique, A. Naeem, P. Westerhoff, S. Mustafa, and A. Alum, "Comparison of different methods for the point of zero charge determination of NiO," *Industrial and Engineering Chemistry Research*, vol. 50, no. 17, pp. 10017–10023, Sep. 2011, doi: 10.1021/ie200271d.
- [13] R. Dillert, A. Engel, J. Große, P. Lindner, and D. W. Bahnemann, "Light intensity dependence of the kinetics of the photocatalytic oxidation of nitrogen(ii) oxide at the surface of TiO<sub>2</sub>," *Physical Chemistry Chemical Physics*, vol. 15, no. 48, pp. 20876–20886, Dec. 2013, doi: 10.1039/c3cp54469a.
- [14] U. I. Gaya and A. H. Abdullah, "Heterogeneous photocatalytic degradation of organic contaminants over titanium dioxide: A review of fundamentals, progress and problems," *Journal of Photochemistry and Photobiology C: Photochemistry Reviews*, vol. 9, no. 1, pp. 1–12, Mar. 2008. doi: 10.1016/j.jphotochemrev.2007.12.003.
- [15] J. G. Herrmann, "<title>Research to protect water infrastructure: EPA's water security research program</title>," in *Optics and Photonics in Global Homeland Security*, May 2005, vol. 5781, pp. 48–52. doi: 10.1117/12.606957.
- [16] U. I. Gaya and A. H. Abdullah, "Heterogeneous photocatalytic degradation of organic contaminants over titanium dioxide: A review of fundamentals, progress and problems," *Journal of Photochemistry and Photobiology C: Photochemistry Reviews*, vol. 9, no. 1, pp. 1–12, Mar. 2008. doi: 10.1016/j.jphotochemrev.2007.12.003.
- [17] S. G. Kumar and L. G. Devi, "Review on modified TiO<sub>2</sub> photocatalysis under UV/visible light: Selected results and related mechanisms on interfacial charge carrier transfer dynamics," *Journal of Physical*

- Chemistry A*, vol. 115, no. 46. pp. 13211–13241, Nov. 24, 2011. doi: 10.1021/jp204364a.
- [18] T. T. T. Huyen, T. T. K. Chi, N. D. Dung, H. Kosslick, and N. Q. Liem, “Enhanced photocatalytic activity of {110}-faceted TiO<sub>2</sub> rutile nanorods in the photodegradation of hazardous pharmaceuticals,” *Nanomaterials*, vol. 8, no. 5, May 2018, doi: 10.3390/nano8050276.
- [19] L. M. Ahmed, A. F. Alkaim, A. F. Halbus, and F. H. Hussein, “Photocatalytic hydrogen production from aqueous methanol solution over metallized TiO<sub>2</sub> Pollution AND NUTRITION View project ultrasonic synthesis of WO<sub>3</sub>/TiO<sub>2</sub> as green technique View project.” [Online]. Available: <https://www.researchgate.net/publication/312062501>
- [20] J. Wang *et al.*, “Enhanced visible-light photodegradation of fluoroquinolone-based antibiotics and *E. coli* growth inhibition using Ag-TiO<sub>2</sub> nanoparticles,” *RSC Advances*, vol. 11, no. 23, pp. 13980–13991, Apr. 2021, doi: 10.1039/d0ra10403e.
- [21] M. Xie, Y. Feng, Y. Luan, X. Fu, and L. Jing, “Facile synthesis of N-doped TiO<sub>2</sub> and its enhanced photocatalytic activity for degrading colorless pollutants,” *Chempluschem*, vol. 79, no. 5, pp. 737–742, 2014, doi: 10.1002/cplu.201400021.
- [22] M. Khairy and W. Zakaria, “Effect of metal-doping of TiO<sub>2</sub> nanoparticles on their photocatalytic activities toward removal of organic dyes,” *Egyptian Journal of Petroleum*, vol. 23, no. 4, pp. 419–426, Dec. 2014, doi: 10.1016/j.ejpe.2014.09.010.
- [23] H. M. Mousa, J. F. Alenezi, I. M. A. Mohamed, A. S. Yasin, A. F. M. Hashem, and A. Abdal-hay, “Synthesis of TiO<sub>2</sub>@ZnO heterojunction for dye photodegradation and wastewater treatment,” *Journal of Alloys and Compounds*, vol. 886, Dec. 2021, doi: 10.1016/j.jallcom.2021.161169.
- [24] D. Zhao *et al.*, “Surface modification of TiO<sub>2</sub> by phosphate: Effect on photocatalytic activity and mechanism implication,” *Journal of Physical Chemistry C*, vol. 112, no. 15, pp. 5993–6001, Apr. 2008, doi: 10.1021/jp712049c.
- [25] Y. Ye, H. Bruning, W. Liu, H. Rijnaarts, and D. Yntema, “Effect of dissolved natural organic matter on the photocatalytic micropollutant removal performance of TiO<sub>2</sub> nanotube array,” *Journal of*

- Photochemistry and Photobiology A: Chemistry*, vol. 371, pp. 216–222, Feb. 2019, doi: 10.1016/j.jphotochem.2018.11.012.
- [26] R. Liu *et al.*, “Recent advancements in g-C<sub>3</sub>N<sub>4</sub>-based photocatalysts for photocatalytic CO<sub>2</sub> reduction: A mini review,” *RSC Advances*, vol. 10, no. 49. Royal Society of Chemistry, pp. 29408–29418, Aug. 11, 2020. doi: 10.1039/d0ra05779g.
- [27] X. Wang *et al.*, “A metal-free polymeric photocatalyst for hydrogen production from water under visible light,” *Nature Materials*, vol. 8, no. 1, pp. 76–80, 2009, doi: 10.1038/nmat2317.
- [28] H. G. Petersen, D. Soelvason, J. W. Perram, E. R. Smith, D. M. Teter, and R. J. Hemley, “God-dard II, *ibid.*,” Gaussian, Inc, 1994. [Online]. Available: <https://www.science.org>
- [29] L. Fang, H. Ohfuji, T. Shinmei, and T. Irifune, “Experimental study on the stability of graphitic C<sub>3</sub>N<sub>4</sub> under high pressure and high temperature,” *Diamond and Related Materials*, vol. 20, no. 5–6, pp. 819–825, May 2011, doi: 10.1016/j.diamond.2011.03.034.
- [30] G. Nabi *et al.*, “Synthesis of g-C<sub>3</sub>N<sub>4</sub> nanorods for visible-light photocatalytic degradation of methylene blue, methylene orange and rhodamine-B,” *International Journal of Environmental Analytical Chemistry*, 2020, doi: 10.1080/03067319.2020.1849666.
- [31] Y. Yang, J. Chen, Z. Mao, N. An, D. Wang, and B. D. Fahlman, “Ultrathin g-C<sub>3</sub>N<sub>4</sub> nanosheets with an extended visible-light-responsive range for significant enhancement of photocatalysis,” *RSC Advances*, vol. 7, no. 4, pp. 2333–2341, 2017, doi: 10.1039/c6ra26172h.
- [32] Y. Hong *et al.*, “A direct one-step synthesis of ultrathin g-C<sub>3</sub>N<sub>4</sub> nanosheets from thiourea for boosting solar photocatalytic H<sub>2</sub> evolution,” *International Journal of Hydrogen Energy*, vol. 44, no. 14, pp. 7194–7204, Mar. 2019, doi: 10.1016/j.ijhydene.2019.01.274.
- [33] X. Fan, Z. Xing, Z. Shu, L. Zhang, L. Wang, and J. Shi, “Improved photocatalytic activity of g-C<sub>3</sub>N<sub>4</sub> derived from cyanamide-urea solution,” *RSC Advances*, vol. 5, no. 11, pp. 8323–8328, 2015, doi: 10.1039/c4ra16362a.
- [34] E. Alwin, K. Kočí, R. Wojcieszak, M. Zieliński, M. Edelmannová, and M. Pietrowski, “Influence of high temperature synthesis on the structure of graphitic carbon nitride and its hydrogen generation

- ability," *Materials*, vol. 13, no. 12, pp. 1–19, Jun. 2020, doi: 10.3390/ma13122756.
- [35] M. Faisal, M. Jalalah, F. A. Harraz, A. M. El-Toni, A. Khan, and M. S. Al-Assiri, "Au nanoparticles-doped g-C<sub>3</sub>N<sub>4</sub> nanocomposites for enhanced photocatalytic performance under visible light illumination," *Ceramics International*, vol. 46, no. 14, pp. 22090–22101, Oct. 2020, doi: 10.1016/j.ceramint.2020.05.250.
- [36] Y. Ma, L. Yang, Y. Yang, Y. Peng, Y. Wei, and Z. Huang, "Multifunctional Ag-decorated g-C<sub>3</sub>N<sub>4</sub> nanosheets as recyclable SERS substrates for CV and RhB detection," *RSC Advances*, vol. 8, no. 39, pp. 22095–22102, 2018, doi: 10.1039/c8ra02657b.
- [37] Y. Jiang, Z. Lin, Y. Zhang, Y. Lai, D. Liang, and C. Yang, "Facile synthesis of porous C-doped C<sub>3</sub>N<sub>4</sub>: Fast charge separation and enhanced photocatalytic hydrogen evolution," *New Journal of Chemistry*, vol. 44, no. 41, pp. 17891–17898, Nov. 2020, doi: 10.1039/d0nj04169f.
- [38] W. Yu, D. Xu, and T. Peng, "Enhanced photocatalytic activity of g-C<sub>3</sub>N<sub>4</sub> for selective CO<sub>2</sub> reduction to CH<sub>3</sub>OH via facile coupling of ZnO: A direct Z-scheme mechanism," *Journal of Materials Chemistry A*, vol. 3, no. 39, pp. 19936–19947, Aug. 2015, doi: 10.1039/c5ta05503b.
- [39] C. Wang, G. Zhang, H. Zhang, Z. Li, and Y. Wen, "One-pot synthesis of porous g-C<sub>3</sub>N<sub>4</sub> nanosheets with enhanced photocatalytic activity under visible light," *Diamond and Related Materials*, vol. 116, Jun. 2021, doi: 10.1016/j.diamond.2021.108416.
- [40] Y. Yang, J. Chen, Z. Mao, N. An, D. Wang, and B. D. Fahlman, "Ultrathin g-C<sub>3</sub>N<sub>4</sub> nanosheets with an extended visible-light-responsive range for significant enhancement of photocatalysis," *RSC Advances*, vol. 7, no. 4, pp. 2333–2341, 2017, doi: 10.1039/c6ra26172h.
- [41] X. Zhang, X. Xie, H. Wang, J. Zhang, B. Pan, and Y. Xie, "Enhanced photoresponsive ultrathin graphitic-phase C<sub>3</sub>N<sub>4</sub> nanosheets for bioimaging," *J Am Chem Soc*, vol. 135, no. 1, pp. 18–21, Jan. 2013, doi: 10.1021/ja308249k.
- [42] Q. Lin, L. Li, S. Liang, M. Liu, J. Bi, and L. Wu, "Efficient synthesis of monolayer carbon nitride 2D nanosheet with tunable concentration and enhanced visible-light photocatalytic activities," *Applied Catalysis*

- B: Environmental*, vol. 163, pp. 135–142, 2015, doi: 10.1016/j.apcatb.2014.07.053.
- [43] F. Dong, Z. Wang, Y. Sun, W. K. Ho, and H. Zhang, “Engineering the nanoarchitecture and texture of polymeric carbon nitride semiconductor for enhanced visible light photocatalytic activity,” *Journal of Colloid and Interface Science*, vol. 401, pp. 70–79, Jul. 2013, doi: 10.1016/j.jcis.2013.03.034.
- [44] P. Niu, L. Zhang, G. Liu, and H. M. Cheng, “Graphene-like carbon nitride nanosheets for improved photocatalytic activities,” *Advanced Functional Materials*, vol. 22, no. 22, pp. 4763–4770, Nov. 2012, doi: 10.1002/adfm.201200922.
- [45] F. Dong, Z. Wang, Y. Sun, W. K. Ho, and H. Zhang, “Engineering the nanoarchitecture and texture of polymeric carbon nitride semiconductor for enhanced visible light photocatalytic activity,” *Journal of Colloid and Interface Science*, vol. 401, pp. 70–79, Jul. 2013, doi: 10.1016/j.jcis.2013.03.034.
- [46] J. Liu, T. Zhang, Z. Wang, G. Dawson, and W. Chen, “Simple pyrolysis of urea into graphitic carbon nitride with recyclable adsorption and photocatalytic activity,” *Journal of Materials Chemistry*, vol. 21, no. 38, pp. 14398–14401, Oct. 2011, doi: 10.1039/c1jm12620b.
- [47] M. Zhang, J. Xu, R. Zong, and Y. Zhu, “Enhancement of visible light photocatalytic activities via porous structure of g-C<sub>3</sub>N<sub>4</sub>,” *Applied Catalysis B: Environmental*, vol. 147, pp. 229–235, Apr. 2014, doi: 10.1016/j.apcatb.2013.09.002.
- [48] F. He, G. Chen, Y. Yu, Y. Zhou, Y. Zheng, and S. Hao, “The sulfur-bubble template-mediated synthesis of uniform porous g-C<sub>3</sub>N<sub>4</sub> with superior photocatalytic performance,” *Chemical Communications*, vol. 51, no. 2, pp. 425–427, Jan. 2015, doi: 10.1039/c4cc07106a.
- [49] S. Sun *et al.*, “Mesoporous graphitic carbon nitride (g-C<sub>3</sub>N<sub>4</sub>) nanosheets synthesized from carbonated beverage-reformed commercial melamine for enhanced photocatalytic hydrogen evolution,” *Materials Chemistry Frontiers*, vol. 3, no. 4, pp. 597–605, Apr. 2019, doi: 10.1039/c8qm00577j.
- [50] Y. Y. Li *et al.*, “Strategy to boost catalytic activity of polymeric carbon nitride: Synergistic effect of controllable: In situ surface engineering

- and morphology,” *Nanoscale*, vol. 11, no. 35, pp. 16393–16405, Sep. 2019, doi: 10.1039/c9nr05413h.
- [51] S. Kumar, A. Kumar, A. Kumar, R. Balaji, and V. Krishnan, “Highly Efficient Visible Light Active 2D-2D Nanocomposites of N-ZnO-g-C<sub>3</sub>N<sub>4</sub> for Photocatalytic Degradation of Diverse Industrial Pollutants,” *ChemistrySelect*, vol. 3, no. 6, pp. 1919–1932, Feb. 2018, doi: 10.1002/slct.201703156.
- [52] V. H. Nguyen *et al.*, “Effective photocatalytic activity of sulfate-modified BiVO<sub>4</sub> for the decomposition of methylene blue under LED visible light,” *Materials*, vol. 12, no. 7, 2019, doi: 10.3390/ma12172681.
- [53] J. Ren, X. Liu, L. Zhang, Q. Liu, R. Gao, and W. L. Dai, “Thermal oxidative etching method derived graphitic C<sub>3</sub>N<sub>4</sub>: Highly efficient metal-free catalyst in the selective epoxidation of styrene,” *RSC Advances*, vol. 7, no. 9, pp. 5340–5348, 2017, doi: 10.1039/c6ra26137j.
- [54] P. Niu, L. Zhang, G. Liu, and H. M. Cheng, “Graphene-like carbon nitride nanosheets for improved photocatalytic activities,” *Advanced Functional Materials*, vol. 22, no. 22, pp. 4763–4770, Nov. 2012, doi: 10.1002/adfm.201200922.
- [55] A. Alaghmandfard and K. Ghandi, “A Comprehensive Review of Graphitic Carbon Nitride (g-C<sub>3</sub>N<sub>4</sub>)–Metal Oxide-Based Nanocomposites: Potential for Photocatalysis and Sensing,” *Nanomaterials*, vol. 12, no. 2. MDPI, Jan. 01, 2022. doi: 10.3390/nano12020294.
- [56] B. v. Lotsch *et al.*, “Unmasking melon by a complementary approach employing electron diffraction, solid-state NMR spectroscopy, and theoretical calculations - Structural characterization of a carbon nitride polymer,” *Chemistry - A European Journal*, vol. 13, no. 17, pp. 4969–4980, 2007, doi: 10.1002/chem.200601759.
- [57] A. Thomas *et al.*, “Graphitic carbon nitride materials: Variation of structure and morphology and their use as metal-free catalysts,” *Journal of Materials Chemistry*, vol. 18, no. 41, pp. 4893–4908, 2008, doi: 10.1039/b800274f.
- [58] P. Niu, L. Zhang, G. Liu, and H. M. Cheng, “Graphene-like carbon nitride nanosheets for improved photocatalytic activities,” *Advanced*

- Functional Materials*, vol. 22, no. 22, pp. 4763–4770, Nov. 2012, doi: 10.1002/adfm.201200922.
- [59] Y. Yang, J. Chen, Z. Mao, N. An, D. Wang, and B. D. Fahlman, “Ultrathin g-C<sub>3</sub>N<sub>4</sub> nanosheets with an extended visible-light-responsive range for significant enhancement of photocatalysis,” *RSC Advances*, vol. 7, no. 4, pp. 2333–2341, 2017, doi: 10.1039/c6ra26172h.
- [60] S. P. Pattnaik, A. Behera, S. Martha, R. Acharya, and K. Parida, “Facile synthesis of exfoliated graphitic carbon nitride for photocatalytic degradation of ciprofloxacin under solar irradiation,” *Journal of Materials Science*, vol. 54, no. 7, pp. 5726–5742, Apr. 2019, doi: 10.1007/s10853-018-03266-x.
- [61] B. Zhang, Q. Wang, J. Zhuang, S. Guan, and B. Li, “Molten salt assisted in-situ synthesis of TiO<sub>2</sub>/g-C<sub>3</sub>N<sub>4</sub> composites with enhanced visible-light-driven photocatalytic activity and adsorption ability,” *Journal of Photochemistry and Photobiology A: Chemistry*, vol. 362, pp. 1–13, Jul. 2018, doi: 10.1016/j.jphotochem.2018.05.009.
- [62] Q. Wang, S. Guan, and B. Li, “2D graphitic-C<sub>3</sub>N<sub>4</sub> hybridized with 1D flux-grown Na-modified K<sub>2</sub>Ti<sub>6</sub>O<sub>13</sub> nanobelts for enhanced simulated sunlight and visible-light photocatalytic performance,” *Catalysis Science and Technology*, vol. 7, no. 18, pp. 4064–4078, 2017, doi: 10.1039/c7cy01134b.
- [63] F. Dong, Z. Wang, Y. Sun, W. K. Ho, and H. Zhang, “Engineering the nanoarchitecture and texture of polymeric carbon nitride semiconductor for enhanced visible light photocatalytic activity,” *Journal of Colloid and Interface Science*, vol. 401, pp. 70–79, Jul. 2013, doi: 10.1016/j.jcis.2013.03.034.
- [64] Z. Y. Bian, Y. Q. Zhu, J. X. Zhang, A. Z. Ding, and H. Wang, “Visible-light driven degradation of ibuprofen using abundant metal-loaded BiVO<sub>4</sub> photocatalysts,” *Chemosphere*, vol. 117, no. 1, pp. 527–531, 2014, doi: 10.1016/j.chemosphere.2014.09.017.
- [65] “1-s2.0-S0021951785710524-main (1)”.
- [66] A. Rashidzadeh, H. Ghafari, and Z. Rezazadeh, “Improved Visible-Light Photocatalytic Activity of g-C<sub>3</sub>N<sub>4</sub>/CuWO<sub>4</sub> Nanocomposite for Degradation of Methylene Blue,” Jan. 2020, p. 43. doi: 10.3390/ecsoc-23-06597.

- [67] B. Liang, Y. Rao, and X. Duan, "The electrical properties and modulation of g-C<sub>3</sub>N<sub>4</sub>/β-As and g-C<sub>3</sub>N<sub>4</sub>/β-Sb heterostructures: A first principles study," *RSC Advances*, vol. 9, no. 66, pp. 38724–38729, 2019, doi: 10.1039/c9ra06357a.
- [68] D. Zhang, Y. Tang, X. Qiu, J. Yin, C. Su, and X. Pu, "Use of synergistic effects of the co-catalyst, p-n heterojunction, and porous structure for improvement of visible-light photocatalytic H<sub>2</sub> evolution in porous Ni<sub>2</sub>O<sub>3</sub>/Mn<sub>0.2</sub>Cd<sub>0.8</sub>S/Cu<sub>3</sub>P@Cu<sub>2</sub>S," *Journal of Alloys and Compounds*, vol. 845, Dec. 2020, doi: 10.1016/j.jallcom.2020.155569.
- [69] L. Zhang, Z. Dai, G. Zheng, Z. Yao, and J. Mu, "Superior visible light photocatalytic performance of reticular BiVO<sub>4</sub> synthesized: Via a modified sol-gel method," *RSC Advances*, vol. 8, no. 19, pp. 10654–10664, 2018, doi: 10.1039/c8ra00554k.
- [70] D. Das, S. L. Shinde, and K. K. Nanda, "Temperature-Dependent Photoluminescence of g-C<sub>3</sub>N<sub>4</sub>: Implication for Temperature Sensing," *ACS Applied Materials and Interfaces*, vol. 8, no. 3, pp. 2181–2186, Jan. 2016, doi: 10.1021/acsami.5b10770.
- [71] J. Yang *et al.*, "Synthesis and characterization of nitrogen-rich carbon nitride nanobelts by pyrolysis of melamine," *Applied Physics A: Materials Science and Processing*, vol. 105, no. 1, pp. 161–166, Oct. 2011, doi: 10.1007/s00339-011-6471-4.
- [72] P. Li, W. Zhang, Y. Zhang, Y. Sun, and F. Dong, "(NH<sub>4</sub>)<sub>2</sub>SO<sub>4</sub>-assisted polycondensation of dicyandiamide for porous g-C<sub>3</sub>N<sub>4</sub> with enhanced photocatalytic NO removal," *RSC Advances*, vol. 6, no. 98, pp. 96334–96338, 2016, doi: 10.1039/c6ra19740j.
- [73] Z. Teng *et al.*, "Edge-Functionalized g-C<sub>3</sub>N<sub>4</sub> Nanosheets as a Highly Efficient Metal-free Photocatalyst for Safe Drinking Water," *Chem*, vol. 5, no. 3, pp. 664–680, Mar. 2019, doi: 10.1016/j.chempr.2018.12.009.
- [74] P. S. Konstas, I. Konstantinou, D. Petrakis, and T. Albanis, "Synthesis, characterization of g-C<sub>3</sub>N<sub>4</sub>/SrTiO<sub>3</sub> heterojunctions and photocatalytic activity for organic pollutants degradation," *Catalysts*, vol. 8, no. 11, Nov. 2018, doi: 10.3390/catal8110554.
- [75] J. Yu and L. Qi, "Template-free fabrication of hierarchically flower-like tungsten trioxide assemblies with enhanced visible-light-driven

photocatalytic activity,” *Journal of Hazardous Materials*, vol. 169, no. 1–3, pp. 221–227, Sep. 2009, doi: 10.1016/j.jhazmat.2009.03.082.

[76] “Coefficient\_of\_determination”.

[77] J. Zhuang *et al.*, “Photocatalytic degradation of RhB over TiO<sub>2</sub> bilayer films: Effect of defects and their location,” *Langmuir*, vol. 26, no. 12, pp. 9686–9694, Jun. 2010, doi: 10.1021/la100302m.



